



Depolarization ratio of smoke and volcanic ash aerosol particles at 1565 nm using a HALO Doppler lidar

Maria Filioglou¹, Krista Luoma², Eija Asmi², Viet Le², Klaus Haikarainen², David Brus², Tero Mielonen¹, Mika Komppula¹, Annele Virtanen³, Olli Sippula³, Iida Pullinen³, Angela Buchholz³, Pasi Miettinen³, Snehitha Kommula³, Saara Peltokorpi³, Liqing Hao³, Kajar Köster³, Annika Saarto⁴, Sanna Pätsi⁴, Pieter G. van Zyl⁵, Liezl Bredekamp⁵, and Ville Vakkari^{2,5}

¹Finnish Meteorological Institute, Atmospheric Research Centre of Eastern Finland, Kuopio, Finland

²Finnish Meteorological Institute, Helsinki, Finland

³Department of Technical Physics, University of Eastern Finland, Kuopio, Finland

⁴Department of Biodiversity Sciences, University of Turku, Turku, Finland

⁵Atmospheric Chemistry Research Group, Chemical Resource Beneficiation, North-West University, Potchefstroom, South Africa

Correspondence: Maria Filioglou (maria.filioglou@fmi.fi)

Abstract. Particle linear depolarization ratio is a widely used parameter in lidar research to distinguish different aerosol types and the thermodynamic phase of water. It is most frequently measured at ultraviolet and visible wavelengths (355 and 532 nm), yet multi-wavelength observations suggest that this parameter can vary substantially with wavelength. In this work, we assessed particle linear depolarization ratios at 1565 nm using Halo Photonics StreamLine Doppler lidars. We examined the depolarization ratio through three case studies featuring extremely fresh and aged smoke, and volcanic ash aerosol particles in the troposphere. Both fresh and aged smoke aerosol particles induced low values. Specifically, aerosol layers dominated by extremely fresh smoke showed a depolarization ratio of 0.017 ± 0.004 , whereas aged long-range transported smoke particles exhibited marginally higher values. Volcanic aerosol layers induced high depolarization ratios with layer mean values of 0.45 ± 0.01 . For the extremely fresh smoke case, we further estimated the smoke mass concentration using the lidar observations at 1565 nm and found good agreement with the in situ observations. These results demonstrate that Halo Doppler lidars operating at 1565 nm wavelength are capable of distinguishing several key aerosol types and can therefore assist in the characterization of atmospheric aerosols.

1 Introduction

Aerosol particles exert a profound influence on climate, yet their effects remain among the largest sources of uncertainty in quantifying anthropogenic forcing (IPCC, 2021). Despite substantial advances driven by field measurements, laboratory studies, and modeling, the magnitude of this uncertainty has remained largely unchanged over the past two decades, with estimates of aerosol effective radiative forcing being far less constrained than those of greenhouse gases (Kahn et al., 2023). Reducing this uncertainty requires, as a fundamental first step, to reliably detect aerosol particles in the atmosphere and accurately characterize their properties. Active remote sensing techniques, particularly lidars (Ansmann et al., 1990), provide this dual



20 capability by first identifying the vertical distribution of aerosol particles and subsequently enabling the retrieval of intrinsic
aerosol properties. One such property is the ratio of cross- to co-polarized signal known as the particle linear depolarization
ratio (δ). This parameter has long been recognized as a powerful indicator of particle shape, allowing discrimination between
spherical and non-spherical aerosol particles (Schotland et al., 1971; Sugimoto et al., 2002; Tesche et al., 2009), thereby offer-
ing critical insights into aerosol type characterization (Nicolae et al., 2018; Papagiannopoulos et al., 2018; Floutsi et al., 2024)
25 and their individual role in air quality, interaction with clouds, and radiative forcing (Noh et al., 2012; Donovan et al., 2015;
Xian et al., 2020; Cairo et al., 2024; Papayannis et al., 2025).

Historically, aerosol measurements on δ using lidars have been conducted across a wide range of wavelengths from ultra-
violet (355 nm) and visible (532 nm) to less commonly used wavelengths at near-infrared (710 nm, 1064 nm) (Sugimoto and
Lee, 2006; Ansmann et al., 2009; Freudenthaler et al., 2009; Tesche et al., 2011; Groß et al., 2013; Pappalardo et al., 2013;
30 Burton et al., 2015). Recent developments have expanded δ observations at 458 nm (Kong et al., 2022), and at longer wave-
lengths, including 808 nm (González et al., 2025), 910 nm (Bedoya-Velásquez et al., 2022) and 1565 nm (Vakkari et al., 2021).
As an outcome, extensive ground-based and airborne campaigns at several locations have established reference δ values for
key aerosol types like mineral dust (Sugimoto and Lee, 2006; Groß et al., 2011; Filioglou et al., 2020), volcanic ash particles
(Ansmann et al., 2010; Pisani et al., 2012; Shimizu et al., 2025), pollen (Bohlmann et al., 2021; Filioglou et al., 2023), ma-
35 rine (Haarig et al., 2017) and smoke aerosol particles (Murayama et al., 2004; Müller et al., 2005). These studies conclude
that non-spherical aerosol particles such as mineral dust, volcanic ash and pollen can maintain high depolarization ratio at
longer wavelengths, while smoke and marine aerosols typically induce much lower depolarization ratio, presenting similar or
decreasing values with increasing wavelength.

Despite these advances, several gaps remain. Long-term, harmonized datasets at longer wavelengths (particularly 910, 1064
40 and 1565 nm) are only beginning to be systematically explored and the spectral dependence of δ for many natural aerosol
types and mixtures of these require further investigation, particularly under varying relative humidity (RH) conditions and
in under-sampled regions. Moreover, case studies demonstrate that δ and its spectral dependence is sensitive to particle size,
shape, composition and mixing state. For example, Freudenthaler et al. (2009) studied Saharan desert dust aerosols at 532 and
1064 nm and concluded that δ tend to be slightly lower at 532 nm compared to the longer wavelength. In contrast, Sugimoto and
45 Lee (2006) concluded the opposite for Asian dust particles. In line with Freudenthaler et al. (2009), Vakkari et al. (2021) and
Haarig et al. (2022) found that mineral dust δ values are slightly lower at 355 and 532 nm compared to the longer wavelengths
of 1565 and 1064 nm, respectively. For pollen aerosol particles, Filioglou et al. (2023) concluded that birch pollen particles
induce higher δ at 910 and 1565 nm compared to 355 and 532 nm. The opposite is valid for pine pollen particles. They also
found that δ is concentration depended, therefore, the longer wavelengths offer an advantage in the detection of large particles
50 such as pollen particles. For marine and polluted marine aerosols, previous studies report a decreasing trend in δ with increasing
wavelength (Vakkari et al., 2021; Haarig et al., 2025). Moreover, Haarig et al. (2018) studied tropospheric smoke particles and
found that they induce a less than 3% δ at 355, 532 and 1064 nm, while higher δ values were reported for stratospheric smoke
layers at shorter wavelengths (Burton et al., 2015; Haarig et al., 2018; Hu et al., 2019). To the authors' knowledge, there are no
studies of δ at 1565 nm for volcanic ash and smoke aerosol particles.



55 Multi-wavelength lidar observations, obtained from single or multiple instruments, promise more reliable characterization
of aerosol properties and aerosol typing. To this direction, the objective of this study is to estimate δ for smoke and volcanic
ash particles using a Halo Doppler lidar operating at 1565 nm. We also extend the applicability of such lidars and estimate
the mass concentration of smoke aerosols at 1565 nm wavelength. In turn, estimating smoke mass concentration from lidars
is valuable because it provides vertically-resolved, model-ready aerosol mass information that improves the representation of
60 smoke loading, plume dynamics, and radiative effects in atmospheric models (Benedetti et al., 2009; Sekiyama et al., 2010;
Zhang et al., 2014). The study closes the current gap in δ datasets at 1565 nm wavelength and facilitates the integration of
this wavelength into operational aerosol monitoring networks. Aerosol observations at 1565 nm benefit from the near absence
of molecular scattering and absorption, which greatly simplifies signal processing and implementation within observational
networks.

65 2 Materials and Methods

Three field campaigns were conducted over the years of 2024, 2020 and 2016 at three different locations: at a Boreal forest site
at Kiviniemi, Finland (62°29'06.0" N, 27°29'27.4" E, 110 m above sea level), at an urban site at Kumpula (Helsinki), Finland
(60°12'13.5" N, 24°57'39.1" E, 45 m a.s.l.) and at a grassland savanna site at Welgegund, South Africa (26°34'11.3" S,
26°56'21.5" E, 1480 m a.s.l.), respectively. In each location, a HALO Photonics Streamline Doppler lidar was operating. To
70 characterize the δ_{1565} of extremely fresh and aged smoke as well as volcanic ash particles, three representative case studies, one
from each field campaign, were selected and presented in Sect. 3. The extremely fresh smoke case was observed in Kiviniemi
(FI), the aged smoke case in Kumpula (FI) and the volcanic ash case in Welgegund (SA). For the extremely fresh smoke
case in Kiviniemi (FI), a suite of ground- and drone-based in situ instruments were employed to quantify aerosol physical
and chemical properties to support the mass concentration estimation of smoke from the lidar observations. To exclude the
75 influence of biological particles on the analysis, given that the measurements in Kiviniemi (FI) coincided with the active pollen
season, a Burkard sampler was operated to monitor airborne pollen concentrations in the near-by station in the city of Kuopio
(62°53'31.5" N, 27°38'01.0" E).

2.1 Lidar observations

Halo Photonics StreamLine lidars are commercially available pulsed Doppler lidars that operate at 1565 nm wavelength (Pear-
80 son et al., 2009). Here, we use Halo Doppler lidars that are equipped with a cross-polar receiver channel, which enables consec-
utive measurement of co- and cross-polar signals and subsequent retrieval of particle linear depolarization ratio (Vakkari et al.,
2021). The lidars were configured with 30 m vertical resolution and focus was set to 2000 m. Other technical specifications
were identical to Vakkari et al. (2021).

At Kumpula (FI) and Welgegund (SA), the Halo Doppler lidars used were capable of full hemispheric scanning. At Kiviniemi
85 (FI), the version with limited scanning (i.e. StreamLine Pro) was used. In this study, we utilize only the vertically-pointing
measurements. At Kiviniemi, the vertically-pointing integration time was set to 7 s per ray and 13 min out of every 15 min was



vertically-pointing measurement. At Kumpula, the vertically-pointing integration time was set to 3.5 s per ray and 8 min out of every 15 min was vertically-pointing measurement. At Welgegend, the vertically-pointing integration time was set to 7 s per ray and 6 min out of every 15 min was vertically-pointing measurement.

90 For each Halo Doppler lidar the data was post-processed following Vakkari et al. (2019). Instrument and campaign specific bleed-through was determined from liquid cloud base observations similar to Le et al. (2024). For Kiviniemi (FI), a bleed-through of 0.0165 ± 0.010 was determined. For Kumpula (FI), bleed-through was determined as 0.00715 ± 0.0028 . For Welgegend (SA), bleed-through was determined as 0.0085 ± 0.007 . These values are in good agreement with the long-term statistics in Le et al. (2024).

95 At 1565 nm wavelength, the molecular backscatter contribution is about 2 orders of magnitude lower than at 532 nm, being approximately $1.9 \times 10^{-8} \text{ m}^{-1} \text{ sr}^{-1}$ at standard pressure and temperature (Bucholtz, 1995). Additionally, in the absence of hydrometeors, the atmospheric transmittance is very close to unity (Vakkari et al., 2021). Therefore, δ_{1565} as derived directly from the instrument after correcting for the bleed-through, can be regarded as a reasonable approximation of the particle linear depolarization ratio, obtained without applying a correction for the molecular scattering contribution, especially during high
100 aerosol load conditions. Similar assumption is valid for the attenuated backscatter coefficient which represents the particle backscatter coefficient, hereafter, β_{1565} .

2.2 Particle mass concentration from lidar observations

Lidar-derived mass concentration (m) has been estimated using the methodology presented in Ansmann et al. (2011). The method requires the mass particle density (ρ), the extinction-to-volume conversion factor (c_v), and the particle extinction
105 coefficient $\alpha = \beta(\lambda) \cdot LR(\lambda)$ for a specific aerosol type at a certain wavelength (λ) to be known according to $m = \rho \cdot c_v(\lambda) \cdot \alpha(\lambda)$. Above, LR stands for the Lidar Ratio, and a density of $\rho = 1.35 \pm 0.05 \text{ g cm}^{-3}$ was used for smoke particles (Reid et al., 2005).

To derive the mass concentration, we first converted the β_{1565} into β_{532} by using a Backscatter-related Ångström exponent (BAE) according to $\beta_{532} = \beta_{1565} \cdot (532/1565)^{-BAE}$. The BAE , as well as, the LR s at both 532 and 1565 nm wavelengths
110 were estimated through Mie calculations (see Sect. 2.4). This wavelength conversion enables us to use a literature value of $0.16 \pm 0.01 e^{-12} \text{ Mm}$ for c_v at 532 nm (Ansmann et al., 2021), which has not been determined at 1565 nm wavelength, making the mass concentration estimation possible.

2.3 In situ aerosol observations

For the extremely fresh smoke event in Kiviniemi (FI), additional ground- and drone-based in situ aerosol observations were
115 considered. The aerosol size distribution in size range of 15-710 nm was measured with a Scanning Mobility Particle Sizer (SMPS). The SMPS setup (TSI Inc., Model 3080) consists of a DMA (TSI Inc., Model 3081) and a CPC (TSI Inc., Model 3776) and temporal resolution was 3 minutes. Aerosol particle size distribution in the range between 0.45 and 15.5 μm was measured using an optical particle counter sensor (OPC-N2, Alphasense Ltd.; e.g., Crilley et al. (2018); Hagan and Kroll (2020); Julaha et al. (2025)) mounted onboard a DJI Matrice 600 drone. The OPC was housed within a custom-built module, similar to Brus



120 et al. (2025), designed for uncrewed aerial vehicles. Measurements were obtained by flying the drone horizontally across the smoke plume at multiple altitudes ranging from 50 m to 110 m. There was a total of four flights, at 11:30, 12:00, 16:15 and 16:45 UTC, each lasting up to 20 minutes. Drone data from the first two flights are considered only, as these periods exhibited spatially consistent smoke conditions between the airborne and surface-based observations.

To crosscheck and inter-compare the measurements of OPC and SMPS, the drone platform was positioned adjacent to the measurement station. The inter-comparison was performed at 14:30 - 15:05 UTC and the size distributions from OPC and SMPS were averaged over this period. The intercomparison showed an approximately twofold difference in particle number size distributions, with lower concentrations measured by the OPC on the drone platform than by the SMPS at the measurement station. This discrepancy is not unexpected, given the different measurement principles of the two instruments, their detection efficiencies and the strong spatial and temporal variability within the smoke plume. Sousan et al. (2016) reported that the OPC-N2 performs well in measuring coarse particles but tends to underestimate number concentrations of submicrometer particles, with a detection efficiency of 78% for particles smaller than 0.5 μm .

To derive the complete aerosol size distribution, the SMPS and OPC size distributions (hereafter SMPS-OPC) were averaged over the time intervals during which the OPC was operating (i.e., the flight periods), and the corresponding 10th and 90th percentiles were calculated over these overlapping intervals. From the combined SMPS-OPC aerosol size distribution, the total mass of aerosol particles was estimated using a particle density of 1.35 g cm^{-3} .

To gain a more detailed understanding of the aerosol composition, and particularly the black carbon (BC) and organic aerosol (OA) content during the burning event, ground-based multi-angle absorption photometer (MAAP, model 5012, Thermo Scientific) and aerosol mass spectrometer (AMS, HR-ToF-AMS, Aerodyne Research Inc., DeCarlo et al. (2006)) measurements from the container (Fig. 1c) were used to estimate the BC-to-organic aerosol ratio (BC/OA). MAAP measured dried aerosol particles from the station's main inlet at a flow rate of 7.5 LPM at 1-min time resolution. The aerosol absorption determined by MAAP was converted to BC mass concentration using the default mass absorption cross-section (MAC) of 6.6 m^2g^{-1} . AMS measures the mass concentration of organics, sulfate, nitrate, ammonia and chloride compounds and was operated in EI-V mode (tungsten vaporizer) at 2-min time resolution and. The instrument was calibrated on-site with ammonia sulfate and ammonia nitrate aerosols to determine the ionization efficiency of nitrate particles and relative ionization efficiency (RIE) of ammonia and sulfate. AMS data analysis was performed using standard tools- SQUIRREL v1.65C and PIKA v1.25C in Igor Pro.

All in situ aerosol observations were averaged for 15 min periods to match the temporal resolution in the lidar observations. Regarding the OPC data, only observations inside the smoke plume were considered. For each flight, we derived an average aerosol size distribution by combining measurements across all sampled altitudes.

150 Pollen concentrations were assessed with a Burkard sampler of Hirst design (Hirst, 1952) at Kuopio (62°53'31.5" N 27°38'01.0" E). The site is part of the Finnish pollen network operated by the University of Turku (<https://sites.utu.fi/siitepoly/toiminta/>) and member of the European Aeroallergen Network. For the derivation of the pollen types and their respective concentrations, the recommendations of the European Aeroallergen Society (Galán et al., 2014) were followed to ensure high data



quality. Pollen concentrations were utilized in the extremely fresh smoke case in Kiviniemi (FI). The distance between the two
155 sites is about 50 km.

2.4 Mie calculations of smoke particles

Mie-theory predicts the optical properties of spherical particles (Mie, 1908). Here, Mie model was used to calculate the β and
 α at the lidar wavelengths (355, 532, 1064 and 1565 nm) in order to infer the LR and BAE from the measured in-situ aerosol
particle size distributions. Mie model calculations were done using the Python-package PyMieScatt (ver 1.8.1.) (Sumlin et al.,
160 2018a).

To perform this analysis, the particles were assumed spherical without core-shell structures. A dry aerosol was also assumed,
as the surface relative humidity (RH) remained below 40%. The assumption of spherical particles required for Mie theory is
supported by the low δ in the lidar observations during the smoke event. From the in-situ observations, the average mass
BC/OA-ratio during the plume was approximately 1%.

165 The complex refractive indices used were $1.5+0.0366i$, $1.5+0.0064i$, $1.5+0.0003i$, $1.5+0.0001i$ at 355, 532, 1064, and
1565 nm, respectively. The imaginary part (k) was derived according to Mukherjee et al. (2025), who measured the k for
fresh boreal forest surface smoldering emissions. A wavelength dependence of k was assumed using their measurements at
365 and 550 nm. The methanol soluble fraction accounted for more than 90% of the total organic aerosol mass, and was there-
fore considered representative of the bulk organic aerosol. In contrast, the methanol insoluble fraction was negligible in these
170 fresh emissions. The real part (n) was treated as constant at a value of 1.5 according to Sumlin et al. (2018b), who observed
that the n was independent of the λ and was between 1.5-1.7.

The absorption by BC was taken into account by assuming an externally mixed aerosol. BC size distribution measured in a
chamber for fresh boreal forest surface was used (Peltokorpi et al., 2026; Vakkari et al., 2026). The BC size distribution was
scaled so that the mass of BC matched the BC/OA-ratio (about 1%) of the mass of particles smaller than $1 \mu\text{m}$. The BC density
175 was assumed to be 1.80 g cm^{-3} . The mass of particles smaller than $1 \mu\text{m}$ was estimated from the derived size distribution
assuming density of 1.35 g cm^{-3} . The complex refractive index for BC was defined according to Eqs. (6) and (7) in Kahnert
and Kanngießer (2020).

2.5 FLEXPART airmass trajectories

Air mass history was simulated using the Lagrangian particle dispersion model FLEXPART (FLEXible PARTicle dispersion
180 model) version 11.0 (Bakels et al., 2024). ERA5 reanalysis from European Centre for Medium-Range Weather Forecasts
(ECMWF) was used as meteorological input (Hersbach et al., 2023). The ERA5 input data was retrieved at 1 h temporal, 0.25°
latitude-longitude resolution and for model levels 40 to 137, which corresponds to approximately the lowest 24 km in the
atmosphere. FLEXPART was run in backward simulation mode and potential emission sensitivity (PES) output was saved at
1 h time resolution.

185 For the aged smoke case in Kumpula, Finland on 22 September 2020 the FLEXPART simulation retroplume was released at
height interval of 3 to 4 km above ground level (a.g.l.) and time interval of 18 to 19 UTC, respectively. FLEXPART backward



simulation was computed for 16 days. For the volcanic ash particles in Welgegund, South Africa on 17 December 2016 the FLEXPART simulation retroplume was released at height interval of 2.5 to 3.2 km a.g.l. and time interval of 4 to 5 UTC, corresponding to the lidar observation of the elevated layer. The duration of the FLEXPART backward simulation for this event was 14 days.

2.6 MODIS fire radiative power

The fire radiative power (FRP) product from MODIS Aqua and Terra, collection 6.1, (Giglio et al., 2016) was downloaded through the FIRMS interface for the period 7 to 20 September 2020 covering the area of North America to examine the locations of wildfires in the path of the airmass for the Kumpula case.

3 Results

In this section, we present the observations of extremely fresh and aged smoke and volcanic ash particles. Extremely fresh and aged smoke aerosols were observed in Finland during 2024 and 2020, and volcanic ash particles were observed in South Africa in 2016.

3.1 Case study 1: Extremely fresh smoke

A controlled prescribed burning was conducted on the 6th of June 2024 in Kiviniemi (62°29'06.0" N, 27°29'27.4" E) in North Savo region in Finland (Fig. 1). Approximately 8 hectares of managed boreal forest ecosystem was burned, with the objective of promoting biodiversity. The area is a 35 - 75 year old dry Scots pine (*Pinus sylvestris*) forest, with scattered birch (*Betula* sp.) within the stand. A commercial thinning was carried out in winter 2022, leaving logging residues unevenly distributed across the area. The understory is sparsely vegetated, with dwarf shrubs (*Vaccinium myrtillus*, *V. vitis-idaea*), mosses (*Pleurozium schreberi*), and *Cladonia* lichens dominating the forest floor. The prescribed burning was performed by the Finnish Forest Administration (Metsähallitus) and the fire was allowed to extinguish naturally—mostly within 24 hours, although isolated smoldering persisted for several days after the burning event. The event was a surface fire of low to moderate intensity, with spatially variable severity ranging from low to high. The prescribed burning realized in two events. In the first burning event, the fire started at about 11 UTC south from the measurement container along the horizontal road until the whole southernmost section of the area was burned (Fig. 1b). The wind direction in this first burning was towards north, bringing the smoke plumes towards the measurement site. The second burning event started after 15.30 UTC. The fire was initiated at the easternmost area above the horizontal road and progressed northwards until the rest of the area was burned. The fire was made to progress in a direction against the wind to ensure a better control of the burning.

Figure 2 presents the atmospheric conditions over Kiviniemi, Finland on the 6th of June 2024, as seen by the HALO Doppler lidar on site. Very high values in the β_{1565} profile are seen close to the surface starting at about 11.00 UTC, caused by high concentrations of smoke particles. In this first aerosol layer, which from now on is referred to as the smoke layer, the δ_{1565} is very low (Fig. 2b). The bottom and top boundaries of the smoke layer are also marked with black filled circles. As seen by



the lidar, the smoke layer had its highest extent during the first burning event in which the direction of the wind was towards the lidar instrument and the fire was at its closest proximity to it. The maximum top height of the smoke layer reached at about 220 460 m and the average geometrical extent of it was 120 ± 90 m.

Figure 3 shows the relationship between β_{1565} and δ_{1565} for all height bins inside the smoke layer boundaries. There is a strong relationship between the intensity of β_{1565} and the value of δ_{1565} in which higher β_{1565} results to lower δ_{1565} . Elevated δ_{1565} values are observed by the lidar after 14 UTC. However, at this time due to the location of the active fire the smoke plume direction was not anymore on the instrument's path. This is also evident from the β_{1565} time series. At the same time, 225 the presence of highly depolarizing aerosol particles can be seen in the δ_{1565} time series. Given that a forest fire was ongoing, large fly-ash particles could potentially lead to high δ_{1565} (Martinent et al., 2025; Kalembkiewicz et al., 2018). However, the elevated δ_{1565} layer extends up to 1 km a.g.l., i.e. much higher than the fresh smoke plume at 11–12 UTC. This suggests that it had had time to mix evenly throughout the boundary layer unlike the local smoke emission. To dive further into this, Figure 4 shows the daily evolution of the pollen concentration from a measurement site 50 km away at the city of Kuopio, where the 230 predominant pollen type on that day was pine. The elevated δ_{1565} observed in this study is in line with Filioglou et al. (2023) observations on pine pollen δ_{1565} . Therefore, we attribute the elevated δ_{1565} to regional scale presence of pine pollen in this case.

A mean δ_{1565} of extremely fresh smoke aerosol particles of 0.017 ± 0.004 was estimated accounting for observations having a β_{1565} higher than $30 \text{ Mm}^{-1} \text{sr}^{-1}$. Previous studies on fresh smoke particle detection report low δ due to the dominance of near- 235 spherical morphology or weakly nonspherical aggregates shortly after emission. Typical tropospheric values of 0.01–0.03 at 355 nm, 0.02–0.06 at 532 nm and 0.01–0.02 at 1064 nm for fresh plumes have been previously reported (Nepomuceno Pereira et al., 2014; Haarig et al., 2018; De Rosa et al., 2022). Falling well within the range of δ in shorter wavelengths, the δ_{1565} shows minimal spectral dependence.

3.1.1 Mass concentration estimation

240 Going beyond, the lidar-derived mass concentration was determined following the methodology outlined by (Ansmann et al., 2010). Since there are no observational values on the LR and c_v at 1565 nm, parameters that are needed for the mass concentration calculation, we converted the β_{1565} from the Doppler lidar into β_{532} using a $BAE_{532/1565}$ (See Sect. 2.2). Furthermore, in order to estimate the mass concentration at 532 nm, the $c_{v,532}$ and LR_{532} should be known. A $c_{v,532}$ of $0.16 \pm 0.01 e^{-12} \text{ Mm}$ for fresh smoke has been previously reported in Ansmann et al. (2021) and utilized in this study. A $BAE_{532/1565}$ and LR_{532} of 245 1.22 ± 0.09 and 28 ± 11 sr were estimated from Mie calculations at 532 nm (see Sect. 2.4). The Mie estimated LR s at 355, 532, 1064 and 1565 nm wavelengths for this specific aerosol mixture during the smoke event were 81 ± 13 sr, 28 ± 11 sr, 45 ± 2 sr and 51 ± 7 sr, respectively. Having the LR_{1565} , the determination of the conversion factor at 1565 nm for boreal smoke aerosol particles was then possible, yielding to a mean value of $c_{v,1565} = 0.32 \pm 0.18 e^{-12} \text{ Mm}$.

The estimated lidar-derived mass concentration for the extremely fresh smoke event is presented in Figure 5 and is further 250 compared against SMPS-OPC in situ observations. The lidar and in-situ measurements are in good agreement. Because the fire source was located in close proximity to the measurement site, the smoke concentration exhibited pronounced small-



scale variability, which is apparent in the in situ observations. The vertical lines represent the temporal variability in smoke concentration, expressed as the range between the 10th and 90th percentiles. The temporal evolution of the plume and its vertical structure is also indicated in the lidar observation. The mass concentration is dominated by the amount of the larger aerosol particles and during the two flights moderate differences were captured. The altitude of the airborne measurements was changing between 50 and 100 m a.g.l. The maximum height during the first (second) flight was 70(100) m. During the 1st flight there is greater agreement between the lidar and in situ observation compared to the 2nd flight but at the same time the range of mass concentration is much larger. This discrepancy is expected, given the different sampling volumes and the inhomogeneity of the smoke plume and assumptions in the mass concentration estimation between these two measuring approaches. Lidar-derived mass concentration estimations are bound to 49% uncertainty, assuming a 10% uncertainty in the β_{1565} and the uncertainty of the rest parameters as noted above. From surface and drone observations, the aerosol composition during the fire event was largely dominated by OA, while BC mass fraction contributed less than 1% in the aerosol mixture. Surface fires, which burn at lower combustion temperatures, emit mainly carbonaceous aerosols with characteristics that favor BrC formation (Cahill et al., 2008; Mukherjee et al., 2025; Vakkari et al., 2026), in contrast to the more crown-fire-dominated events in North America (Rogers et al., 2015); this behavior was likewise observed here.

Related to the Mie-estimated LRs , the LR at 355 and 532 nm are consistent with previous measurements of extremely fresh smoke particles exhibiting a decreasing trend (De Rosa et al., 2025), although the Mie-estimated LR_{355} , in this study is larger than the one reported at De Rosa et al. (2025). More often, there is a neutral or slight increasing spectral dependence (Müller et al., 2005; Nicolae et al., 2013; De Rosa et al., 2022; Janicka et al., 2023) reported for fresh smoke. Although there are no literature values for the LR_{1565} , increasing LR_{1064} has been previously reported for long-range transported free-tropospheric smoke layers (Haarig et al., 2018; Su et al., 2025). This is not the case in Sayer et al. (2014) where similar LR values at 355 and 532 nm followed by a decrease towards 1064 nm were reported at boreal locations using observations from a plethora of AERONET sites. To this direction, using light-scattering simulations, Liu and Mishchenko (2020) investigated the lidar ratios at 532 and 1064 nm for a range of refractive indexes, particle sizes and shapes and found a decreasing trend with increasing wavelength for aerosol particles with an effective radius smaller than about $0.3 \mu\text{m}$ as well. In this study, the Mie estimations point to increasing LRs between 1064 and 1565 nm wavelengths but the values are smaller compared to the ones reported in Haarig et al. (2018) and Su et al. (2025), which is attributed to the aging of the smoke particles and the likely higher share of absorbing aerosols like BC in the aerosol mixture in their studies.

The lower LRs estimated from the Mie calculations at the visible and infrared wavelengths could be explained by the contribution of BrC, which absorbs more effectively at shorter wavelengths. Using a laboratory open burning setup Mukherjee et al. (2025) found that optical properties of freshly emitted organic particles are substantially diverse and dependent on the fire type (smoldering, flaming) and burning material. Among others, they used Finnish boreal peat and forest surface samples. Photochemical aging transformed the weakly absorbing particles into less absorbing while the opposite is anticipated in dark-aging conditions. In contrast, BC is more likely to become more absorbing due to the lensing effect Zhang et al. (2018). The wavelength dependence of LR in aged smoke particles ($>$ a few hours) is also related to the composition of the smoke plume as it contains larger aggregates that become optically apparent at longer wavelengths. It is important to emphasize that the



case presented here concerns smoke aerosol particles sampled within a few minutes after emission, whereas most previously reported observations of fresh smoke aerosol layers in the literature present substantially longer timescales (from hours to days). Smoke particles undergo rapid aging within hours after emission altering their size and scattering properties (Kleinman et al., 2020; Saide et al., 2022; Vakkari et al., 2018).

3.2 Case study 2: Long-range transported free tropospheric smoke

On the 22nd of September 2020, free-tropospheric aerosol layers were observed over Kumpula site (60°12'13.5" N, 24°57'39.1" E) in Finland (Fig. 6). The aerosol layers which extended from 1.3 to 5.1 km in the vertical had a variable geometrical depth with a mean value of 800 m (range: 120 m - 2.2 km). An example case of the hourly-averaged Doppler lidar profiles between 17:00 and 18:00 UTC is shown in Fig. 7. Elevated β_{1565} values can be seen at around 1.6 km and between 2.7 and 4 km with a mean δ_{1565} of 0.034 ± 0.01 and 0.038 ± 0.017 , respectively. For this case, the 16-day FLEXPART backward simulation showed air mass transport from California, which overlapped with very intensive fire locations according to MODIS observations (Fig. 8). In fact, long-range transport from the same wildfire episode in California (USA) was observed a few days earlier in Germany (Baars et al., 2021).

To further investigate the variation of δ_{1565} in these long-range transported smoke layers, hourly β_{1565} and δ_{1565} profiles were calculated to enhance the signal-to-noise ratio (SNR). Figure 9 presents the relationship between the hourly-averaged profiles of β_{1565} and δ_{1565} for all height bins inside the smoke layer boundaries. The smoke layer boundaries for the hourly profiles are indicated in the hourly time-height plot that can be found in the appendix (Fig. A1). Similar to the fresh smoke, lower δ_{1565} values coincide with higher β_{1565} . Since this is long-range transported smoke located in the free troposphere, the β_{1565} is lower and the scatter of δ_{1565} is larger than in the extremely fresh smoke case. In order to retrieve the mean δ_{1565} , we have accounted both for the relative uncertainty of δ_{1565} and the intensity of β_{1565} in a way that observations presenting high β_{1565} values and low relative uncertainty in δ_{1565} are weighted more in the average. A weighted mean δ_{1565} of smoke aerosol particles of 0.04 ± 0.02 was estimated for the long-range transported smoke particles. We should note here that the same conclusions are valid when estimating the mean δ_{1565} using the 15 minutes resolution information but the uncertainty is higher due to the poorer SNR (not shown).

Free-tropospheric smoke particles have been reported to produce depolarization ratios below 5% across lidar wavelengths up to 1064 nm (Nepomuceno Pereira et al., 2014; Haarig et al., 2018). The present findings are consistent with these earlier observations. In comparison to the fresh smoke, the free tropospheric smoke δ_{1565} is larger, indicating that the shape of the particles is more non-spherical. Various factors can contribute to the observed difference in δ_{1565} , including higher fraction of fractal-shaped BC in smoke emitted in fires with high FRP or the presence of soil dust in the smoke plumes. Recent findings also link organic aerosol shape changes to chemical aging (Qin et al., 2024).

3.3 Case study 3: Volcanic ash in free troposphere

A free tropospheric aerosol layer with very high δ_{1565} reached the measurement site at Welgegund, South Africa (26°34'11.3" S, 26°56'21.5" E) in the night from 16th December to 17th December 2016. Figure 10 shows the temporal evolution of the layer's



320 β_{1565} (upper panel) and δ_{1565} (lower panel) over the measurement site as monitored by the HALO Doppler lidar. The base and top heights of the layer are marked with circles. The feature between 2.5 and 3.5 km clearly demonstrates the existence of a pronounced aerosol layer and the large values of δ_{1565} are a clear indication of non-spherical particles; a typical feature of volcanic ash (Pisani et al., 2012). Scattered clouds before and after the plume did not prevent the observation of the plume. The plume's altitude remained rather constant during the 12 hour observation period as well as the layer's geometrical thickness of
325 850 m.

FLEXPART air mass history for this layer (Fig. 11) shows substantial contribution from South America and the direction of Copahue Volcano, which is located on the border between Chile and Argentina in the Andes Mountains ($37^{\circ} 45' S$, $71^{\circ} 10.2' W$, 2997 m a.s.l.). Historically, the volcano has exhibited intermittent mild-to-moderate explosive activity, with a notable increase in eruptions since the beginning of 2012. During early December 2016, diffuse gas, water vapor, and ash plumes from
330 Copahue rose to altitudes of 3-3.3 km a.s.l. and were transported eastbound (Paez et al., 2021), which overlaps with the air mass history analysis in Fig. 11. Therefore, we attribute the pronounced high δ_{1565} layer as ash originating from the Copahue Volcano.

Figure 12 presents the hourly extracted lidar information of β_{1565} and δ_{1565} at the volcanic plume layer only (Fig. A1). The color indicates the relative uncertainty of δ_{1565} . In this highly depolarizing aerosol layer, we can define the δ_{1565} with
335 a better than 10% accuracy estimating a depolarization ratio for the volcanic ash aerosols to be 0.46 ± 0.05 at 1565 nm. A δ_{1565} of 0.45 ± 0.01 is estimated using the weighted mean method described in the previous case study. No significant changes were found between the 15 minutes and 1 hour temporal resolutions apart from the higher uncertainty accompanying the finer temporal resolution observations.

3.4 Depolarization ratio at 1565 nm

340 Here we summarize the depolarization ratios of the fresh smoke, aged smoke and volcanic ash aerosol particles from this study. We also gather δ_{1565} information for all studied aerosol particles up-to-date (Table 1). This collection of case studies at 1565 nm for various aerosol types demonstrates that lidar-based classification algorithms could benefit from the extended information at δ_{1565} , distinguishing non-spherical particles from spherical ones. It is evident that the longer wavelength is sensitive to different aerosol types leveraging their usage in classifying aerosols and monitoring air quality.

345 For the three aforementioned aerosol types δ exhibits a wavelength dependence. Specifically, for fresh smoke, depolarization ratios at shorter wavelengths (355 and 532 nm) are typically low due to the near-spherical nature of freshly emitted sub-micron particles; previous multi-wavelength lidar studies report tropospheric smoke depolarization ratios < 0.03 at 355 and 532 nm and 0.01 at 1064 nm; a consistent behavior at 1565 nm was found in this study too, reflecting limited non-sphericity. In aged smoke, particle reshaping and mixing together with the smoke's physical and chemical properties and any co-lifted dust
350 particles can enhance non-sphericity at shorter wavelengths. At longer wavelengths, however, depolarization tends to remain low because small soot aggregates scatter less efficiently, producing a characteristic spectral decline in depolarization with increasing wavelength. In contrast, volcanic ash consists of larger, non-spherical particles that produce high depolarization ratios at both UV and visible wavelengths. Previous studies at 355 and 532 nm report δ of about 0.35–0.38 for ash plumes



with little spectral variation among these shorter wavelengths (Groß et al., 2012). Our findings suggest that this non-sphericity
355 persists at 1565 nm and is further enhanced, presenting an increase of δ with increasing wavelength.

4 Conclusions

For the first time, we report particle linear depolarization ratios for extremely fresh and aged forest fire smoke as well as
volcanic ash at 1565 nm. We found that (a) non-spherical particles such as volcanic ash induce elevated particle linear depo-
larization ratios at 1565 nm, consistent to the previous observations at shorter wavelengths and (b) smoke aerosols, dominated
360 by near-spherical particles, yield lower depolarization ratio, but aged smoke show some variability probably due to differences
in the BC content, dust uplifting and/or processing during the plume transport. We further estimated the mass concentration
of extremely fresh smoke using a combination of Mie-derived optical properties and lidar observations with reasonable agree-
ment to in situ observations. The Mie-estimated lidar ratios increased with increasing wavelength except at 355 nm. Whether
this behavior is characteristic of extremely fresh smoke particles in boreal forest environments and for this type of surface fire
365 remains uncertain; however, previous observational and light-scattering simulations have demonstrated the high sensitivity of
lidar intensive properties such as the lidar ratio to smoke particles.

For the extremely fresh smoke event within the planetary boundary layer, we found very low particle linear depolarization
ratio at 1565 nm of 0.017 ± 0.004 , which is in good agreement with previous observations at 1064 nm showing minimal
wavelength dependence. For long-range transported smoke aerosols in the free troposphere, we observed marginally higher
370 depolarization ratio of 0.04 ± 0.02 . The volcanic ash depolarization ratio induced high values of 0.45 ± 0.01 and combined
with earlier lidar studies at shorter wavelengths it shows an increase with increasing wavelength. Taken together, our findings
show that Halo Doppler lidars provide a valuable additional wavelength information at 1565 nm for investigating the spectral
dependence of particle linear depolarization ratio, even up to the lowest 4-5 km of the atmosphere. Therefore, they build towards
a more accurate aerosol typing and support the development of new aerosol climatologies, thereby enhancing network-wide
375 utilization of aerosol measurements at this wavelength.

Aerosol observations at 1565 nm benefit from the near absence of molecular scattering and absorption, which greatly sim-
plifies signal pre-processing. At this wavelength, Rayleigh scattering is negligible, so the lidar return is dominated by aerosol
particles rather than atmospheric molecules. This provides a clear advantage over the shorter wavelengths and for real-time
application of the observations. However, the trade-off is that the aerosol backscatter efficiency is much lower compared to
380 visible wavelengths, making it harder to detect fine particles and aerosol layers with low concentrations. Furthermore, mixtures
of different aerosol types could also become challenging due to the weaker scattering contrast.

Future work should further investigate aerosol optical and microphysical properties at 1565 nm, as current understanding at
this wavelength emerges from limited case studies. Expanded observational studies with various aerosol mixtures would help
clarify how different aerosol types behave in the near-infrared and how these signatures vary with atmospheric conditions. Such
385 efforts are essential for fully assessing the potential of 1565 nm measurements to complement the traditional lidar wavelengths
and improve aerosol classification efforts.



Data availability. HALO Doppler lidar observations are available through Cloudnet portal (Komppula and O'Connor, 2025). Flexpart version 11.0 is available at <https://gitlab.phaidra.org/flexpart/>. Fire radiative power (FRP) data are publicly available through FIRMS interface at <https://firms.modaps.eosdis.nasa.gov/map/>. In situ aerosol and pollen observations are available upon request.

390 **Appendix A**

A1

Author contributions. MF conceptualized the original paper, performed the main analysis considering all data sources and wrote the manuscript. VV conceptualized the original paper and provided the Halo Doppler lidar observations, FLEXPART air mass trajectories and MODIS fire radiative power data. KL combined the in situ observations from SMPS and OPC instruments, performed and provided the Mie calculations. 395 EA analyzed and provided the MAAP observations. EA and VL analyzed and provided the OPC observations. DB prepared the drone load and VL and KH performed the flights onsite. SK provided the SMPS observations. LH provided the AMS observations. AS and SPä provided the pollen data. All authors were involved in the editing and discussion of the manuscript.

Competing interests. At least one of the (co-)authors is a member of the editorial board of Atmospheric Chemistry and Physics.

Acknowledgements. This study was supported by the Research Council of Finland (grant no 337552, 343359, 369600, 369601). The pre- 400 scribed burning is part of the the project “Climate and air quality impacts of boreal forest fires”, (2023 – 2027) funded by the Jane and Atos Erkko Foundation. The fire area is part of the Life2Taiga project (2022-2028) funded by the European Union’s LIFE Nature and Biodiversity programme, which aims to restore forests in Finland and Sweden through conservation burning. We acknowledge the use of data from NASA’s Fire Information for Resource Management System (FIRMS) part of NASA’s Land, Atmosphere Near real-time Capability for Earth observations (LANCE) and NASA’s Earth Science Data and Information System (ESDIS).



405 References

- Ansmann, A., Riebesell, M., and Weitkamp, C.: Measurement of atmospheric aerosol extinction profiles with a Raman lidar, *Opt. Lett.*, 15, 746–748, <https://doi.org/10.1364/OL.15.000746>, 1990.
- Ansmann, A., Baars, H., Tesche, M., Müller, D., Althausen, D., Engelmann, R., Pauliquevis, T., and Artaxo, P.: Dust and smoke transport from Africa to South America: Lidar profiling over Cape Verde and the Amazon rainforest, *Geophysical Research Letters*, 36, <https://doi.org/https://doi.org/10.1029/2009GL037923>, 2009.
- 410 Ansmann, A., Tesche, M., Groß, S., Freudenthaler, V., Seifert, P., Hiebsch, A., Schmidt, J., Wandinger, U., Mattis, I., Müller, D., and Wiegner, M.: The 16 April 2010 major volcanic ash plume over central Europe: EARLINET lidar and AERONET photometer observations at Leipzig and Munich, Germany, *Geophysical Research Letters*, 37, <https://doi.org/https://doi.org/10.1029/2010GL043809>, 2010.
- Ansmann, A., Tesche, M., Seifert, P., Groß, S., Freudenthaler, V., Apituley, A., Wilson, K. M., Serikov, I., Linné, H., Heinold, B., Hiebsch, A., Schnell, F., Schmidt, J., Mattis, I., Wandinger, U., and Wiegner, M.: Ash and fine-mode particle mass profiles from EARLINET-AERONET observations over central Europe after the eruptions of the Eyjafjallajökull volcano in 2010, *Journal of Geophysical Research: Atmospheres*, 116, <https://doi.org/10.1029/2010JD015567>, 2011.
- 415 Ansmann, A., Ohneiser, K., Mamouri, R.-E., Knopf, D. A., Veselovskii, I., Baars, H., Engelmann, R., Foth, A., Jimenez, C., Seifert, P., and Barja, B.: Tropospheric and stratospheric wildfire smoke profiling with lidar: mass, surface area, CCN, and INP retrieval, *Atmospheric Chemistry and Physics*, 21, 9779–9807, <https://doi.org/10.5194/acp-21-9779-2021>, 2021.
- 420 Baars, H., Radenz, M., Floutsis, A. A., Engelmann, R., Althausen, D., Heese, B., Ansmann, A., Flament, T., Dabas, A., Trapon, D., Reitebuch, O., Bley, S., and Wandinger, U.: Californian Wildfire Smoke Over Europe: A First Example of the Aerosol Observing Capabilities of Aeolus Compared to Ground-Based Lidar, *Geophysical Research Letters*, 48, e2020GL092194, <https://doi.org/https://doi.org/10.1029/2020GL092194>, 2021.
- 425 Bakels, L., Tatsii, D., Tipka, A., Thompson, R., Dütsch, M., Blaschek, M., Seibert, P., Baier, K., Bucci, S., Cassiani, M., Eckhardt, S., Groot Zwaafink, C., Henne, S., Kaufmann, P., Lechner, V., Maurer, C., Mulder, M. D., Pissò, I., Plach, A., Subramanian, R., Vojta, M., and Stohl, A.: FLEXPART version 11: improved accuracy, efficiency, and flexibility, *Geoscientific Model Development*, 17, 7595–7627, <https://doi.org/10.5194/gmd-17-7595-2024>, 2024.
- Bedoya-Velásquez, A. E., Hoyos-Restrepo, M., Barreto, A., García, R. D., Romero-Campos, P. M., García, O., Ramos, R., Roininen, R., Toledano, C., Sicard, M., and Ceolato, R.: Estimation of the Mass Concentration of Volcanic Ash Using Ceilometers: Study of Fresh and Transported Plumes from La Palma Volcano, *Remote Sensing*, 14, <https://doi.org/10.3390/rs14225680>, 2022.
- 430 Benedetti, A., Morcrette, J.-J., Boucher, O., Dethof, A., Engelen, R. J., Fisher, M., Flentje, H., Huneeus, N., Jones, L., Kaiser, J. W., Kinne, S., Mangold, A., Razinger, M., Simmons, A. J., and Suttie, M.: Aerosol analysis and forecast in the ECMWF Integrated Forecast System: 2. Data assimilation, *Atmospheric Chemistry and Physics*, 9, 6717–6733, <https://doi.org/10.5194/acp-9-6717-2009>, 2009.
- 435 Bohlmann, S., Shang, X., Vakkari, V., Giannakaki, E., Leskinen, A., Lehtinen, K. E. J., Pätsi, S., and Komppula, M.: Lidar depolarization ratio of atmospheric pollen at multiple wavelengths, *Atmospheric Chemistry and Physics*, 21, 7083–7097, <https://doi.org/10.5194/acp-21-7083-2021>, 2021.
- Brus, D., Le, V., Kuula, J., and Douglgeris, K.: Data collected by a drone backpack for air quality and atmospheric state measurements during Pallas Cloud Experiment 2022 (PaCE2022), *Earth System Science Data*, 17, 5209–5219, <https://doi.org/10.5194/essd-17-5209-2025>, 2025.
- 440



- Bucholtz, A.: Rayleigh-scattering calculations for the terrestrial atmosphere, *Appl. Opt.*, 34, 2765–2773, <https://doi.org/10.1364/AO.34.002765>, 1995.
- Burton, S. P., Hair, J. W., Kahnert, M., Ferrare, R. A., Hostetler, C. A., Cook, A. L., Harper, D. B., Berkoff, T. A., Seaman, S. T., Collins, J. E., Fenn, M. A., and Rogers, R. R.: Observations of the spectral dependence of linear particle depolarization ratio of aerosols using NASA
445 Langley airborne High Spectral Resolution Lidar, *Atmospheric Chemistry and Physics*, 15, 13 453–13 473, <https://doi.org/10.5194/acp-15-13453-2015>, 2015.
- Cahill, C. F., Cahill, T. A., and Perry, K. D.: The size- and time-resolved composition of aerosols from a sub-Arctic boreal forest prescribed burn, *Atmospheric Environment*, 42, 7553–7559, <https://doi.org/https://doi.org/10.1016/j.atmosenv.2008.04.034>, 2008.
- Cairo, F., Di Liberto, L., Dionisi, D., and Snels, M.: Understanding Aerosol-Cloud Interactions through Lidar Techniques: A Review, *Remote
450 Sensing*, 16, <https://doi.org/10.3390/rs16152788>, 2024.
- Crilly, L. R., Shaw, M., Pound, R., Kramer, L. J., Price, R., Young, S., Lewis, A. C., and Pope, F. D.: Evaluation of a low-cost optical particle counter (Alphasense OPC-N2) for ambient air monitoring, *Atmospheric Measurement Techniques*, 11, 709–720, <https://doi.org/10.5194/amt-11-709-2018>, 2018.
- De Rosa, B., Amato, F., Amodeo, A., D’Amico, G., Dema, C., Falconieri, A., Giunta, A., Gumà-Claramunt, P., Kampouri, A., Solomos, S.,
455 Mytilinaios, M., Papagiannopoulos, N., Summa, D., Veselovskii, I., and Mona, L.: Characterization of Extremely Fresh Biomass Burning Aerosol by Means of Lidar Observations, *Remote Sensing*, 14, <https://doi.org/10.3390/rs14194984>, 2022.
- De Rosa, B., Amodeo, A., D’Amico, G., Papagiannopoulos, N., Rosoldi, M., Veselovskii, I., Cardellicchio, F., Falconieri, A., Gumà-Claramunt, P., Laurita, T., Mytilinaios, M., Papanikolaou, C.-A., Amodio, D., Colangelo, C., Di Girolamo, P., Gandolfi, I., Giunta, A., Lapenna, E., Marra, F., Petracca Altieri, R. M., Ripepi, E., Summa, D., Volini, M., Arienzo, A., and Mona, L.: Characterization of Fresh
460 and Aged Smoke Particles Simultaneously Observed with an ACTRIS Multi-Wavelength Raman Lidar in Potenza, Italy, *Remote Sensing*, 17, <https://doi.org/10.3390/rs17152538>, 2025.
- DeCarlo, P. F., Kimmel, J. R., Trimborn, A., Northway, M. J., Jayne, J. T., Aiken, A. C., Gonin, M., Fuhrer, K., Horvath, T., Docherty, K. S., Worsnop, D. R., and Jimenez, J. L.: Field-deployable, high-resolution, time-of-flight aerosol mass spectrometer, *Analytical Chemistry*, 78, 8281–8289, <https://doi.org/10.1021/ac061249n>, 2006.
- 465 Donovan, D. P., Klein Baltink, H., Henzing, J. S., de Roode, S. R., and Siebesma, A. P.: A depolarisation lidar-based method for the determination of liquid-cloud microphysical properties, *Atmospheric Measurement Techniques*, 8, 237–266, <https://doi.org/10.5194/amt-8-237-2015>, 2015.
- EU: CORINE Land Cover 2018 (raster 100 m), Europe, 6-yearly version 2020 20u1, <https://sdi.eea.europa.eu/catalogue/copernicus/api/records/960998c1-1870-4e82-8051-6485205ebbac?language=all>, accessed: 14 November 2025, 2025.
- 470 Filioglou, M., Giannakaki, E., Backman, J., Kesti, J., Hirsikko, A., Engelmann, R., O’Connor, E., Leskinen, J. T. T., Shang, X., Korhonen, H., Lihavainen, H., Romakkaniemi, S., and Komppula, M.: Optical and geometrical aerosol particle properties over the United Arab Emirates, *Atmospheric Chemistry and Physics*, 20, 8909–8922, <https://doi.org/10.5194/acp-20-8909-2020>, 2020.
- Filioglou, M., Leskinen, A., Vakkari, V., O’Connor, E., Tuononen, M., Tuominen, P., Laukkanen, S., Toiviainen, L., Saarto, A., Shang, X., Tiitta, P., and Komppula, M.: Spectral dependence of birch and pine pollen optical properties using a synergy of lidar instruments,
475 *Atmospheric Chemistry and Physics*, 23, 9009–9021, <https://doi.org/10.5194/acp-23-9009-2023>, 2023.
- Floutsi, A. A., Baars, H., and Wandinger, U.: HETEAC-Flex: an optimal estimation method for aerosol typing based on lidar-derived intensive optical properties, *Atmospheric Measurement Techniques*, 17, 693–714, <https://doi.org/10.5194/amt-17-693-2024>, 2024.



- Freudenthaler, V., Esselborn, M., Wiegner, M., Heese, B., Tesche, M., Ansmann, A., Müller, D., Althausen, D., Wirth, M., Fix, A., Ehret, G., Knippertz, P., Toledano, C., Gasteiger, J., Garhammer, M., and Seefeldner, M.: Depolarization ratio profiling at several wavelengths in pure Saharan dust during SAMUM 2006, *Tellus B*, 61, 165–179, <https://doi.org/10.1111/j.1600-0889.2008.00396.x>, 2009.
- Galán, C., Smith, M., Thibaudon, M., Frenguelli, G., Oteros, J., Gehrig, R., Berger, U., Clot, B., Brandao, R., and Group, E. Q. W.: Pollen monitoring: minimum requirements and reproducibility of analysis, *Aerobiologia*, 30, 385–395, <https://doi.org/10.1007/s10453-014-9335-5>, 2014.
- Giglio, L., Schroeder, W., and Justice, C. O.: The collection 6 MODIS active fire detection algorithm and fire products, *Remote Sensing of Environment*, 178, 31–41, <https://doi.org/10.1016/j.rse.2016.02.054>, published in final edited form 11 Mar 2016, 2016.
- González, Y., Sánchez-Barrero, M. F., Popovici, I., Barreto, A., Victori, S., Welton, E. J., García, R. D., Sicilia, P. G., Almansa, F. A., Torres, C., and Goloub, P.: Compact dual-wavelength depolarization lidar for aerosol characterization over the subtropical North Atlantic, *Atmospheric Measurement Techniques*, 18, 1885–1908, <https://doi.org/10.5194/amt-18-1885-2025>, 2025.
- Groß, S., Tesche, M., Freudenthaler, V., Toledano, C., Wiegner, M., Ansmann, A., Althausen, D., and Seefeldner, M.: Characterization of Saharan dust, marine aerosols and mixtures of biomass-burning aerosols and dust by means of multi-wavelength depolarization and Raman lidar measurements during SAMUM 2, *Tellus B: Chemical and Physical Meteorology*, 63, 706–724, <https://doi.org/10.1111/j.1600-0889.2011.00556.x>, 2011.
- Groß, S., Freudenthaler, V., Wiegner, M., Gasteiger, J., Geiß, A., and Schnell, F.: Dual-wavelength linear depolarization ratio of volcanic aerosols: Lidar measurements of the Eyjafjallajökull plume over Maisach, Germany, *Atmospheric Environment*, 48, 85–96, <https://doi.org/10.1016/j.atmosenv.2011.06.017>, volcanic ash over Europe during the eruption of Eyjafjallajökull on Iceland, April-May 2010, 2012.
- Groß, S., Esselborn, M., Abicht, F., Wirth, M., Fix, A., and Minikin, A.: Airborne high spectral resolution lidar observation of pollution aerosol during EUCAARI-LONGREX, *Atmospheric Chemistry and Physics*, 13, 2435–2444, <https://doi.org/10.5194/acp-13-2435-2013>, 2013.
- Haarig, M., Ansmann, A., Gasteiger, J., Kandler, K., Althausen, D., Baars, H., Radenz, M., and Farrell, D. A.: Dry versus wet marine particle optical properties: RH dependence of depolarization ratio, backscatter, and extinction from multiwavelength lidar measurements during SALTRACE, *Atmospheric Chemistry and Physics*, 17, 14 199–14 217, <https://doi.org/10.5194/acp-17-14199-2017>, 2017.
- Haarig, M., Ansmann, A., Baars, H., Jimenez, C., Veselovskii, I., Engelmann, R., and Althausen, D.: Depolarization and lidar ratios at 355, 532, and 1064nm and microphysical properties of aged tropospheric and stratospheric Canadian wildfire smoke, *Atmospheric Chemistry and Physics*, 18, 11 847–11 861, <https://doi.org/10.5194/acp-18-11847-2018>, 2018.
- Haarig, M., Ansmann, A., Engelmann, R., Baars, H., Toledano, C., Torres, B., Althausen, D., Radenz, M., and Wandinger, U.: First triple-wavelength lidar observations of depolarization and extinction-to-backscatter ratios of Saharan dust, *Atmospheric Chemistry and Physics*, 22, 355–369, <https://doi.org/10.5194/acp-22-355-2022>, 2022.
- Haarig, M., Engelmann, R., Baars, H., Gast, B., Althausen, D., and Ansmann, A.: Discussion of the spectral slope of the lidar ratio between 355 nm and 1064 nm from multiwavelength Raman lidar observations, *EGUsphere*, 2025, 1–35, <https://doi.org/10.5194/egusphere-2025-449>, 2025.
- Hagan, D. H. and Kroll, J. H.: Assessing the accuracy of low-cost optical particle sensors using a physics-based approach, *Atmospheric Measurement Techniques*, 13, 6343–6355, <https://doi.org/10.5194/amt-13-6343-2020>, 2020.



- Hersbach, H., Bell, B., Berrisford, P., Biavati, G., Horányi, A., Muñoz Sabater, J., Nicolas, J., Peubey, C., Radu, R., Rozum, I.,
515 Schepers, D., Simmons, A., Soci, C., Dee, D., and Thépaut, J.-N.: ERA5 hourly data on single levels from 1940 to present,
<https://doi.org/10.24381/cds.adbb2d47>, accessed on 23-Mar-2026, 2023.
- Hirst, J. M.: An automatic volumetric spore trap, *Annals of Applied Biology*, 39, 257–265, <https://doi.org/https://doi.org/10.1111/j.1744-7348.1952.tb00904.x>, 1952.
- Hu, Q., Goloub, P., Veselovskii, I., Bravo-Aranda, J.-A., Popovici, I. E., Podvin, T., Haeffelin, M., Lopatin, A., Dubovik, O., Pietras, C.,
520 Huang, X., Torres, B., and Chen, C.: Long-range-transported Canadian smoke plumes in the lower stratosphere over northern France,
Atmospheric Chemistry and Physics, 19, 1173–1193, <https://doi.org/10.5194/acp-19-1173-2019>, 2019.
- IPCC: Climate Change 2021: The Physical Science Basis. Contribution of Working Group I to the Sixth Assessment Report of the Intergovernmental Panel on Climate Change, vol. In Press, Cambridge University Press, Cambridge, United Kingdom and New York, NY, USA, <https://doi.org/10.1017/9781009157896>, 2021.
- 525 Janicka, L., Davulienė, L., Bycenkiene, S., and Stachlewska, I. S.: Long term observations of biomass burning aerosol over Warsaw by means of multiwavelength lidar, *Opt. Express*, 31, 33 150–33 174, <https://doi.org/10.1364/OE.496794>, 2023.
- Julaha, K., Ždímal, V., Mbengue, S., Brus, D., and Zíková, N.: Drone-based vertical profiling of particulate matter size distribution and carbonaceous aerosols: urban vs. rural environment, *Atmospheric Chemistry and Physics*, 25, 17 933–17 951, <https://doi.org/10.5194/acp-25-17933-2025>, 2025.
- 530 Kahn, R. A., Andrews, E., Brock, C. A., Chin, M., Feingold, G., Gettelman, A., Levy, R. C., Murphy, D. M., Nenes, A., Pierce, J. R., Popp, T., Redemann, J., Sayer, A. M., da Silva, A. M., Sogacheva, L., and Stier, P.: Reducing Aerosol Forcing Uncertainty by Combining Models With Satellite and Within-The-Atmosphere Observations: A Three-Way Street, *Reviews of Geophysics*, 61, e2022RG000 796, <https://doi.org/https://doi.org/10.1029/2022RG000796>, e2022RG000796 2022RG000796, 2023.
- Kahnert, M. and Kanngießler, F.: Modelling optical properties of atmospheric black carbon aerosols, *Journal of Quantitative Spectroscopy and Radiative Transfer*, 244, 106 849, <https://doi.org/https://doi.org/10.1016/j.jqsrt.2020.106849>, 2020.
- 535 Kalemekiewicz, J., Galas, D., and Sitarz-Palczak, E.: The Physicochemical Properties and Composition of Biomass Ash and Evaluating Directions of its Applications, *Polish Journal of Environmental Studies*, 27, 2593–2603, <https://doi.org/10.15244/pjoes/80870>, 2018.
- Kleinman, L. I., Sedlacek III, A. J., Adachi, K., Buseck, P. R., Collier, S., Dubey, M. K., Hodshire, A. L., Lewis, E., Onasch, T. B., Pierce, J. R., Shilling, J., Springston, S. R., Wang, J., Zhang, Q., Zhou, S., and Yokelson, R. J.: Rapid evolution of aerosol particles and their optical
540 properties downwind of wildfires in the western US, *Atmospheric Chemistry and Physics*, 20, 13 319–13 341, <https://doi.org/10.5194/acp-20-13319-2020>, 2020.
- Komppula, M. and O’Connor, E.: Doppler lidar data from Kiviniemi on 6 June 2024, ACTRIS Cloud remote sensing data centre unit (CLU), <https://cloudnet.fmi.fi/file/7fc69d32-56df-48d8-ba9d-d302051bc414>, accessed: 2026-03-06, 2025.
- Kong, Z., Yu, J., Gong, Z., Hua, D., and Mei, L.: Visible, near-infrared dual-polarization lidar based on polarization cameras: system design,
545 evaluation and atmospheric measurements, *Opt. Express*, 30, 28 514–28 533, <https://doi.org/10.1364/OE.463763>, 2022.
- Le, V., Lobo, H., O’Connor, E. J., and Vakkari, V.: Long-term aerosol particle depolarization ratio measurements with HALO Photonics Doppler lidar, *Atmospheric Measurement Techniques*, 17, 921–941, <https://doi.org/10.5194/amt-17-921-2024>, 2024.
- Liu, L. and Mishchenko, M. I.: Spectrally dependent linear depolarization and lidar ratios for nonspherical smoke aerosols, *Journal of Quantitative Spectroscopy and Radiative Transfer*, 248, 106 953, <https://doi.org/https://doi.org/10.1016/j.jqsrt.2020.106953>, 2020.
- 550 Martinent, B., Santoni, P.-A., Coppalle, A., Quilichini, Y., and Barboni, T.: Investigation of the morphology and composition of aerosols from plant burning, *Journal of Aerosol Science*, 187, 106 589, <https://doi.org/https://doi.org/10.1016/j.jaerosci.2025.106589>, 2025.



- Mie, G.: Beiträge zur Optik trüber Medien, speziell kolloidaler Metallösungen, *Annalen der Physik*, 330, 377–445, <https://doi.org/https://doi.org/10.1002/andp.19083300302>, 1908.
- Mukherjee, A., Hartikainen, A., Somero, M., Luostari, V., Ihalainen, M., Rüger, C. P., Kekäläinen, T., Nissinen, V. H., Barreira, L. M. F.,
555 Koponen, H., Kokkola, T., Li, D., Vettikkat, L., Yli-Pirilä, P., Shahzaib, M., Ruppel, M. M., Vakkari, V., Jaars, K., Siebert, S. J., Buchholz, A., Köster, K., van Zyl, P. G., Timonen, H., Kinnunen, N., Jänis, J., Virtanen, A., Virkkula, A., and Sippula, O.: Brown carbon emissions from laboratory combustion of Eurasian arctic-boreal and South African savanna biomass, *Atmospheric Chemistry and Physics*, 25, 16 747–16 774, <https://doi.org/10.5194/acp-25-16747-2025>, 2025.
- Murayama, T., Müller, D., Wada, K., Shimizu, A., Sekiguchi, M., and Tsukamoto, T.: Characterization of Asian dust and
560 Siberian smoke with multi-wavelength Raman lidar over Tokyo, Japan in spring 2003, *Geophysical Research Letters*, 31, <https://doi.org/https://doi.org/10.1029/2004GL021105>, 2004.
- Müller, D., Mattis, I., Wandinger, U., Ansmann, A., Althausen, D., and Stohl, A.: Raman lidar observations of aged Siberian and Canadian forest fire smoke in the free troposphere over Germany in 2003: Microphysical particle characterization, *Journal of Geophysical Research: Atmospheres*, 110, <https://doi.org/https://doi.org/10.1029/2004JD005756>, 2005.
- 565 Nepomuceno Pereira, S., Preißer, J., Guerrero-Rascado, J. L., Silva, A. M., and Wagner, F.: Forest Fire Smoke Layers Observed in the Free Troposphere over Portugal with a Multiwavelength Raman Lidar: Optical and Microphysical Properties, *The Scientific World Journal*, 2014, 421 838, <https://doi.org/https://doi.org/10.1155/2014/421838>, 2014.
- Nicolae, D., Nemuc, A., Müller, D., Talianu, C., Vasilescu, J., Belegante, L., and Kolgotin, A.: Characterization of fresh and aged biomass burning events using multiwavelength Raman lidar and mass spectrometry, *Journal of Geophysical Research: Atmospheres*, 118, 2956–
570 2965, <https://doi.org/https://doi.org/10.1002/jgrd.50324>, 2013.
- Nicolae, D., Vasilescu, J., Talianu, C., Biniotoglou, I., Nicolae, V., Andrei, S., and Antonescu, B.: A neural network aerosol-typing algorithm based on lidar data, *Atmospheric Chemistry and Physics*, 18, 14 511–14 537, <https://doi.org/10.5194/acp-18-14511-2018>, 2018.
- Noh, Y. M., Müller, D., Lee, H., Lee, K., Kim, K., Shin, S., and Kim, Y. J.: Estimation of radiative forcing by the dust and non-dust content in mixed East Asian pollution plumes on the basis of depolarization ratios measured with lidar, *Atmospheric Environment*, 61, 221–231,
575 <https://doi.org/https://doi.org/10.1016/j.atmosenv.2012.07.034>, 2012.
- Paez, P., Cogliati, M., Caselli, A., and Monasterio, A.: An analysis of volcanic SO₂ and ash emissions from Copahue volcano, *Journal of South American Earth Sciences*, 110, 103 365, <https://doi.org/https://doi.org/10.1016/j.jsames.2021.103365>, 2021.
- Papagiannopoulos, N., Mona, L., Amodeo, A., D’Amico, G., Gumà Claramunt, P., Pappalardo, G., Alados-Arboledas, L., Guerrero-Rascado, J. L., Amiridis, V., Kokkalis, P., Apituley, A., Baars, H., Schwarz, A., Wandinger, U., Biniotoglou, I., Nicolae, D., Bortoli,
580 D., Comerón, A., Rodríguez-Gómez, A., Sicard, M., Papayannis, A., and Wiegner, M.: An automatic observation-based aerosol typing method for EARLINET, *Atmospheric Chemistry and Physics*, 18, 15 879–15 901, <https://doi.org/10.5194/acp-18-15879-2018>, 2018.
- Papayannis, A., Soupiona, O., Gidarakou, M., Papanikolaou, C.-A., Anagnou, D., Foskinis, R., Mylonaki, M., Mandelia, K., and Solomos, S.: Optical Properties and Radiative Forcing Estimations of High-Altitude Aerosol Transport During Saharan Dust Events Based on Laser Remote Sensing Techniques (CLIMPACT Campaign 2021, Greece), *Remote Sensing*, 17, <https://doi.org/10.3390/rs17213607>, 2025.
- 585 Pappalardo, G., Mona, L., D’Amico, G., Wandinger, U., Adam, M., Amodeo, A., Ansmann, A., Apituley, A., Alados Arboledas, L., Balis, D., Boselli, A., Bravo-Aranda, J. A., Chaikovskiy, A., Comeron, A., Cuesta, J., De Tomasi, F., Freudenthaler, V., Gausa, M., Giannakaki, E., Giehl, H., Giunta, A., Grigorov, I., Groß, S., Haeffelin, M., Hiebsch, A., Iarlori, M., Lange, D., Linné, H., Madonna, F., Mattis, I., Mamouri, R.-E., McAuliffe, M. A. P., Mitev, V., Molero, F., Navas-Guzman, F., Nicolae, D., Papayannis, A., Perrone, M. R., Pietras, C., Pietruczuk, A., Pisani, G., Preißler, J., Pujadas, M., Rizi, V., Ruth, A. A., Schmidt, J., Schnell, F., Seifert, P., Serikov, I., Sicard, M.,



- 590 Simeonov, V., Spinelli, N., Stebel, K., Tesche, M., Trickl, T., Wang, X., Wagner, F., Wiegner, M., and Wilson, K. M.: Four-dimensional distribution of the 2010 Eyjafjallajökull volcanic cloud over Europe observed by EARLINET, *Atmospheric Chemistry and Physics*, 13, 4429–4450, <https://doi.org/10.5194/acp-13-4429-2013>, 2013.
- Pearson, G., Davies, F., and Collier, C.: An Analysis of the Performance of the UFAM Pulsed Doppler Lidar for Observing the Boundary Layer, *Journal of Atmospheric and Oceanic Technology*, 26, 240 – 250, <https://doi.org/10.1175/2008JTECHA1128.1>, 2009.
- 595 Peltokorpi, S., Kommula, S. M., Buchholz, A., Hao, L., Ihalainen, M., Jaars, K., Köster, K., Rosewig, E. I., Siebert, S. J., Somero, M., Vettikkat, L., Yli-Pirilä, P., van Zyl, P. G., Passig, J., Zimmermann, R., Sippula, O., Vakkari, V., and Virtanen, A.: Savannah and Boreal Biomass Burning as a Source for Cloud Condensation Nuclei, *Journal of Geophysical Research: Atmospheres*, 131, e2025JD044564, <https://doi.org/https://doi.org/10.1029/2025JD044564>, e2025JD044564 2025JD044564, 2026.
- Pisani, G., Boselli, A., Coltelli, M., Leto, G., Pica, G., Scollo, S., Spinelli, N., and Wang, X.: Lidar depolarization measurement of fresh
600 volcanic ash from Mt. Etna, Italy, *Atmospheric Environment*, 62, 34–40, <https://doi.org/https://doi.org/10.1016/j.atmosenv.2012.08.015>, 2012.
- Qin, Z., Wang, H., He, A., Sun, Y., Li, J., Zhang, Y., and Zhang, Q.: Backscattering Linear Depolarization Ratio of Smoke Aerosols From Biomass Burning, *Journal of Geophysical Research: Atmospheres*, 129, e2024JD041276, <https://doi.org/https://doi.org/10.1029/2024JD041276>, e2024JD041276 2024JD041276, 2024.
- 605 Reid, J. S., Koppmann, R., Eck, T. F., and Eleuterio, D. P.: A review of biomass burning emissions part II: intensive physical properties of biomass burning particles, *Atmospheric Chemistry and Physics*, 5, 799–825, <https://doi.org/10.5194/acp-5-799-2005>, 2005.
- Rogers, B., Soja, A., Goulden, M., et al.: Influence of tree species on continental differences in boreal fires and climate feedbacks, *Nature Geoscience*, 8, 228–234, <https://doi.org/10.1038/ngeo2352>, 2015.
- Saide, P. E., Thapa, L. H., Ye, X., Pagonis, D., Campuzano-Jost, P., Guo, H., Schueneman, M. K., Jimenez, J.-L., Moore, R., Wiggins, E.,
610 Winstead, E., Robinson, C., Thornhill, L., Sanchez, K., Wagner, N. L., Ahern, A., Katich, J. M., Perring, A. E., Schwarz, J. P., Lyu, M., Holmes, C. D., Hair, J. W., Fenn, M. A., and Shingler, T. J.: Understanding the Evolution of Smoke Mass Extinction Efficiency Using Field Campaign Measurements, *Geophysical Research Letters*, 49, e2022GL099175, <https://doi.org/https://doi.org/10.1029/2022GL099175>, e2022GL099175 2022GL099175, 2022.
- Sayer, A. M., Hsu, N. C., Eck, T. F., Smirnov, A., and Holben, B. N.: AERONET-based models of smoke-dominated aerosol near source
615 regions and transported over oceans, and implications for satellite retrievals of aerosol optical depth, *Atmospheric Chemistry and Physics*, 14, 11493–11523, <https://doi.org/10.5194/acp-14-11493-2014>, 2014.
- Schotland, R. M., Sassen, K., and Stone, R.: Observations by Lidar of Linear Depolarization Ratios for Hydrometeors, *Journal of Applied Meteorology and Climatology*, 10, 1011 – 1017, [https://doi.org/10.1175/1520-0450\(1971\)010<1011:OBLOLD>2.0.CO;2](https://doi.org/10.1175/1520-0450(1971)010<1011:OBLOLD>2.0.CO;2), 1971.
- Sekiyama, T. T., Tanaka, T. Y., Shimizu, A., and Miyoshi, T.: Data assimilation of CALIPSO aerosol observations, *Atmospheric Chemistry
620 and Physics*, 10, 39–49, <https://doi.org/10.5194/acp-10-39-2010>, 2010.
- Shimizu, A., Nakamichi, H., and Iguchi, M.: Long-Term Lidar Observations of Volcanic Ash from Sakurajima, *Journal of Disaster Research*, 20, 281–286, <https://doi.org/10.20965/jdr.2025.p0281>, 2025.
- Sousan, S., Koehler, K., Hallett, L., and Peters, T. M.: Evaluation of the Alphasense optical particle counter (OPC-N2) and the Grimm portable aerosol spectrometer (PAS-I.108), *Aerosol Science and Technology*, 50, 1352–1365, <https://doi.org/10.1080/02786826.2016.1232859>,
625 2016.
- Su, J., Delgado, R., Berkoff, T. A., Sullivan, J. T., Gronoff, G. P., and Phoenix, D. B.: Observation of fresh wildfire smoke over Hampton, VA in winter, *Atmospheric Environment*, 358, 121370, <https://doi.org/https://doi.org/10.1016/j.atmosenv.2025.121370>, 2025.



- Sugimoto, N. and Lee, C. H.: Characteristics of dust aerosols inferred from lidar depolarization measurements at two wavelengths, *Appl. Opt.*, 45, 7468–7474, <https://doi.org/10.1364/AO.45.007468>, 2006.
- 630 Sugimoto, N., Matsui, I., Shimizu, A., Uno, I., Asai, K., Endoh, T., and Nakajima, T.: Observation of dust and anthropogenic aerosol plumes in the Northwest Pacific with a two-wavelength polarization lidar on board the research vessel Mirai, *Geophysical Research Letters*, 29, 7–1–7–4, <https://doi.org/https://doi.org/10.1029/2002GL015112>, 2002.
- Sumlin, B. J., Heinson, W. R., and Chakrabarty, R. K.: Retrieving the aerosol complex refractive index using PyMieScatt: A Mie computational package with visualization capabilities, *Journal of Quantitative Spectroscopy and Radiative Transfer*, 205, 127–134, <https://doi.org/https://doi.org/10.1016/j.jqsrt.2017.10.012>, 2018a.
- 635 Sumlin, B. J., Heinson, Y. W., Shetty, N., Pandey, A., Pattison, R. S., Baker, S., Hao, W. M., and Chakrabarty, R. K.: UV–Vis–IR spectral complex refractive indices and optical properties of brown carbon aerosol from biomass burning, *Journal of Quantitative Spectroscopy and Radiative Transfer*, 206, 392–398, <https://doi.org/https://doi.org/10.1016/j.jqsrt.2017.12.009>, 2018b.
- Tesche, M., Ansmann, A., Müller, D., Althausen, D., Engelmann, R., Freudenthaler, V., and Groß, S.: Vertically resolved separation of dust and smoke over Cape Verde using multiwavelength Raman and polarization lidars during Saharan Mineral Dust Experiment 2008, *Journal of Geophysical Research: Atmospheres*, 114, <https://doi.org/https://doi.org/10.1029/2009JD011862>, 2009.
- 640 Tesche, M., Gross, S., Ansmann, A., Müller, D., Althausen, D., Freudenthaler, V., and Esselborn, M.: Profiling of Saharan dust and biomass-burning smoke with multiwavelength polarization Raman lidar at Cape Verde, *Tellus B: Chemical and Physical Meteorology*, 63, 649–676, <https://doi.org/10.1111/j.1600-0889.2011.00548.x>, 2011.
- 645 Vakkari, V., Beukes, J. P., Dal Maso, M., Aurela, M., Josipovic, M., Van Zyl, P. G., Tiitta, P., Kulmala, M., and Laakso, L.: Major secondary aerosol formation in southern African open biomass burning plumes, *Nature Geoscience*, 11, 580–583, <https://doi.org/10.1038/s41561-018-0170-0>, 2018.
- Vakkari, V., Manninen, A. J., O’Connor, E. J., Schween, J. H., van Zyl, P. G., and Marinou, E.: A novel post-processing algorithm for Halo Doppler lidars, *Atmospheric Measurement Techniques*, 12, 839–852, <https://doi.org/10.5194/amt-12-839-2019>, 2019.
- 650 Vakkari, V., Baars, H., Böhlmann, S., Bühl, J., Komppula, M., Mamouri, R.-E., and O’Connor, E. J.: Aerosol particle depolarization ratio at 1565 nm measured with a Halo Doppler lidar, *Atmospheric Chemistry and Physics*, 21, 5807–5820, <https://doi.org/10.5194/acp-21-5807-2021>, 2021.
- Vakkari, V., Vettikkat, L., Kommula, S., Mukherjee, A., Hao, L., Backman, J., Buchholz, A., Gawlitta, N., Ihalainen, M., Jaars, K., Köster, K., Le, V., Miettinen, P., Nissinen, A., Czech, H., Alton, M., Passig, J., Peltokorpi, S., Piedehierro, A. A., Pullinen, I., Rosewig, E. I., Schobesberger, S., Shukla, D., Siebert, S. J., Somero, M., Virkkula, A., Welti, A., Yli-Pirilä, P., Ylisirniö, A., Zimmermann, R., van Zyl, P. G., Virtanen, A., and Sippula, O.: Laboratory Experiments on Savannah and European Boreal Forest Fire Emissions, *Journal of Geophysical Research: Atmospheres*, 131, e2025JD044 543, <https://doi.org/https://doi.org/10.1029/2025JD044543>, 2026.
- 655 Xian, J., Sun, D., Xu, W., Han, Y., Zheng, J., Peng, J., and Yang, S.: Urban air pollution monitoring using scanning Lidar, *Environmental Pollution*, 258, 113 696, <https://doi.org/https://doi.org/10.1016/j.envpol.2019.113696>, 2020.
- 660 Zhang, J., Reid, J. S., Westphal, D. L., Baker, N. L., and Hyer, E. J.: A system for operational aerosol optical depth data assimilation over global oceans, *Journal of Geophysical Research: Atmospheres*, 119, 2013JD020 666, <https://doi.org/10.1002/2013JD020666>, 2014.
- Zhang, Y., Favez, O., Canonaco, F., et al.: Evidence of major secondary organic aerosol contribution to lensing effect black carbon absorption enhancement, *npj Climate and Atmospheric Science*, 1, 47, <https://doi.org/10.1038/s41612-018-0056-2>, 2018.

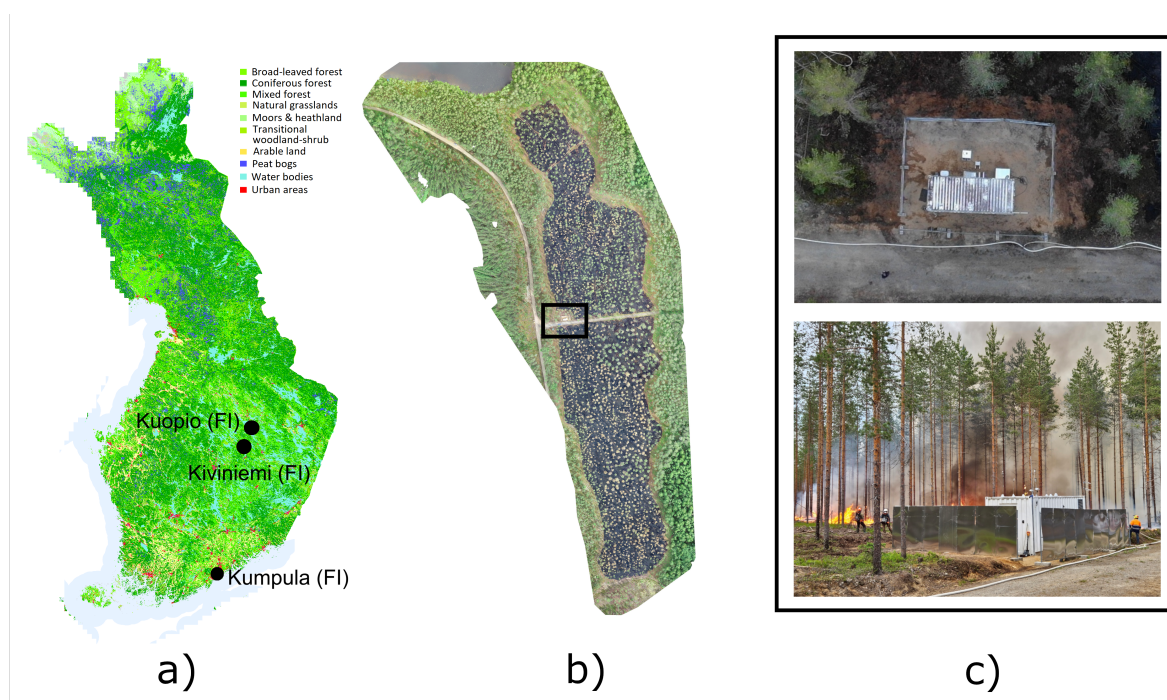


Figure 1. a) Measurement site locations in Finland and land cover from the Copernicus Land Cover inventory CORINE (EU, 2025). b) Aerial view of the burned area at Kiviniemi site. The black rectangle indicates the measurement station. c) Top and side view of the measurement station in Kiviniemi.

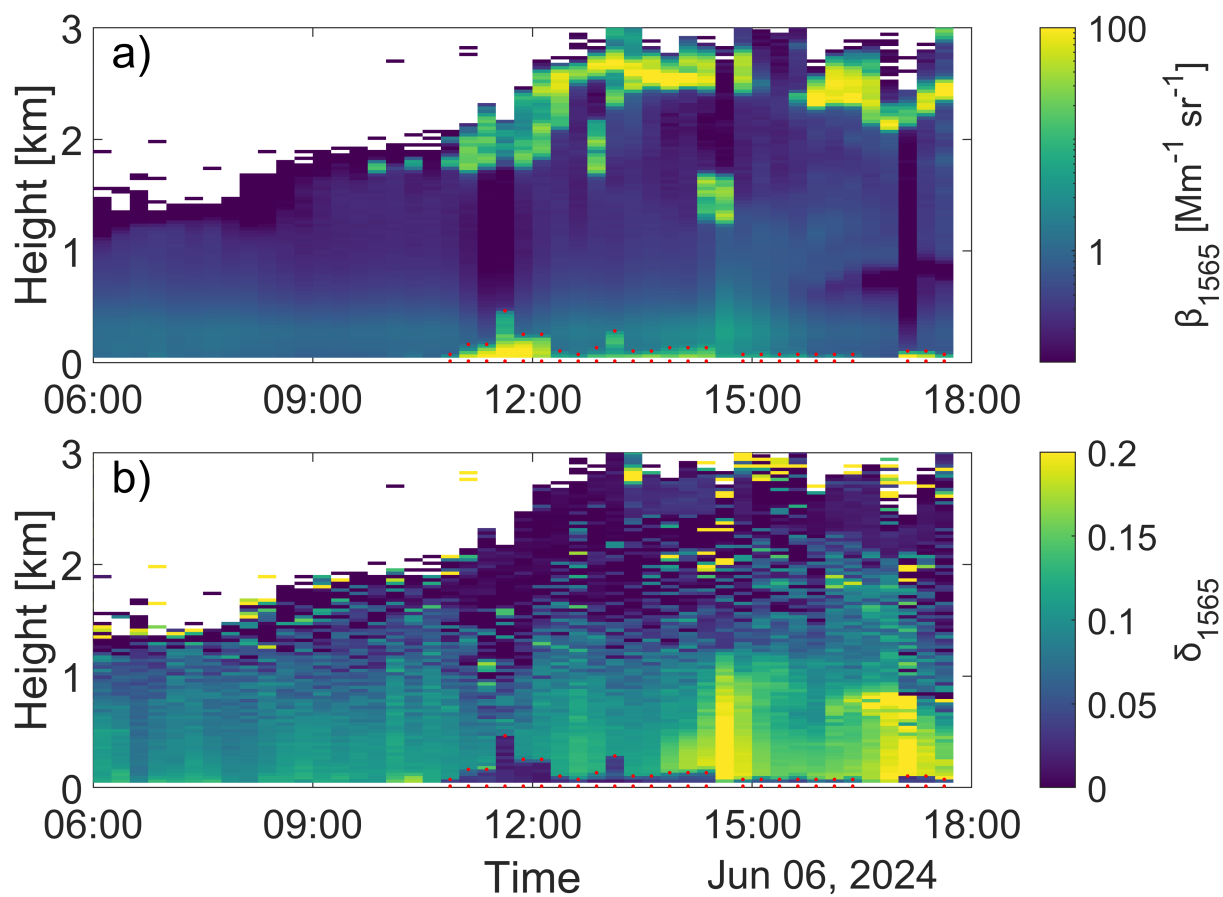


Figure 2. Time-height plot of a) β_{1565} and b) δ_{1565} measured in Kiviniemi 06 June 2024, with the HALO Doppler lidar. The red dots indicate the boundaries of the smoke layer. The temporal resolution corresponds to 15 minutes.

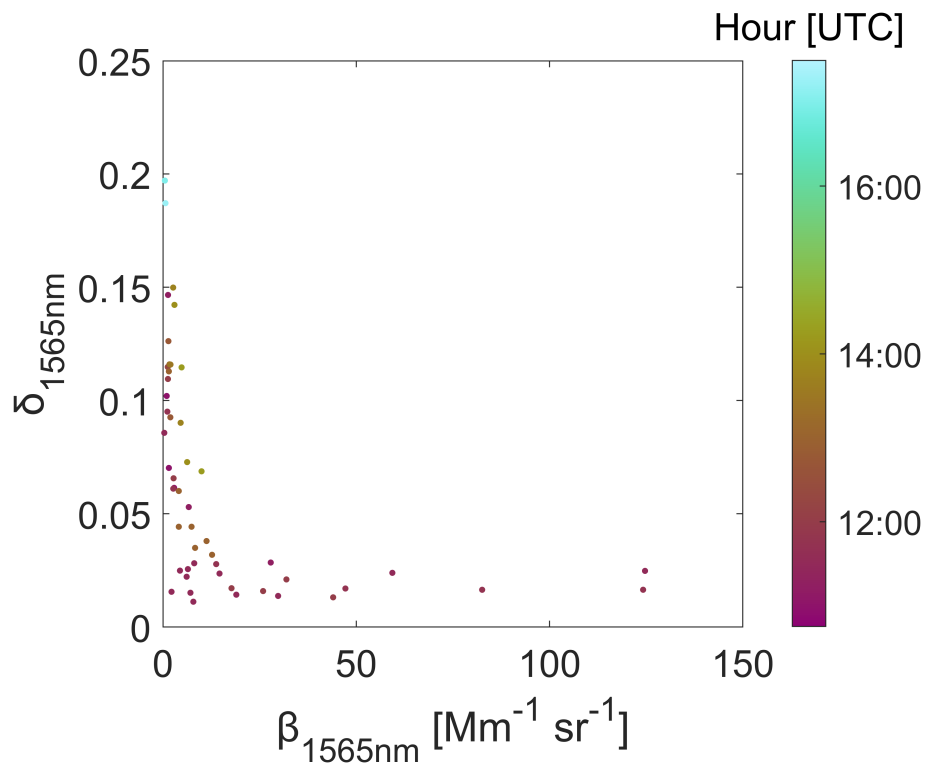


Figure 3. Scatterplot of β_{1565} versus δ_{1565} for all height bins within the boundaries of the smoke layer. The color indicates the time of the observations.

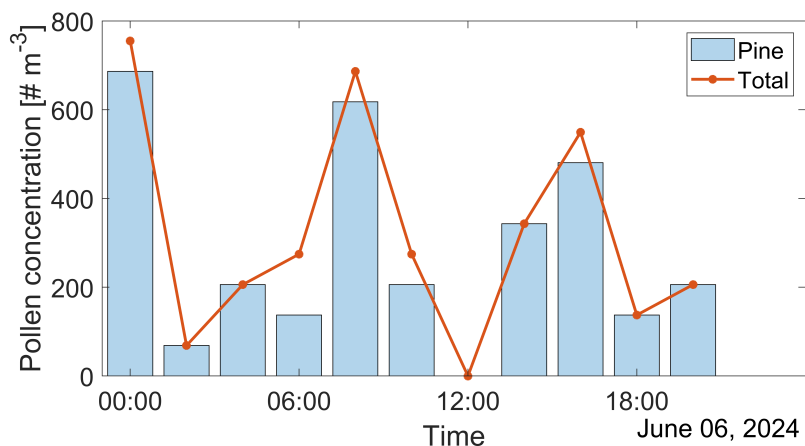


Figure 4. Evolution of the pine and total pollen concentration on the 6th of June 2024 from the Burkard sampler at Kuopio site.

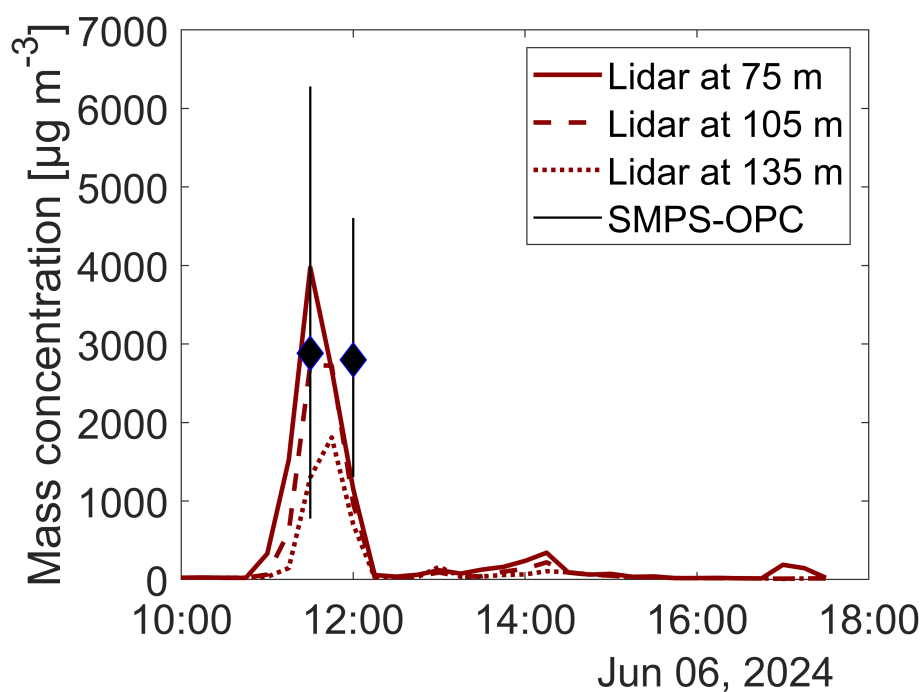


Figure 5. Mass concentration estimations from in situ SMPS-OPC observations and from lidar observations at 75, 105 and 135 m. The SMPS-OPC observations are limited to the drone flight times between 11:30-11:40 and 12:00-12:10. The vertical lines indicate the 10th and 90th percentiles.

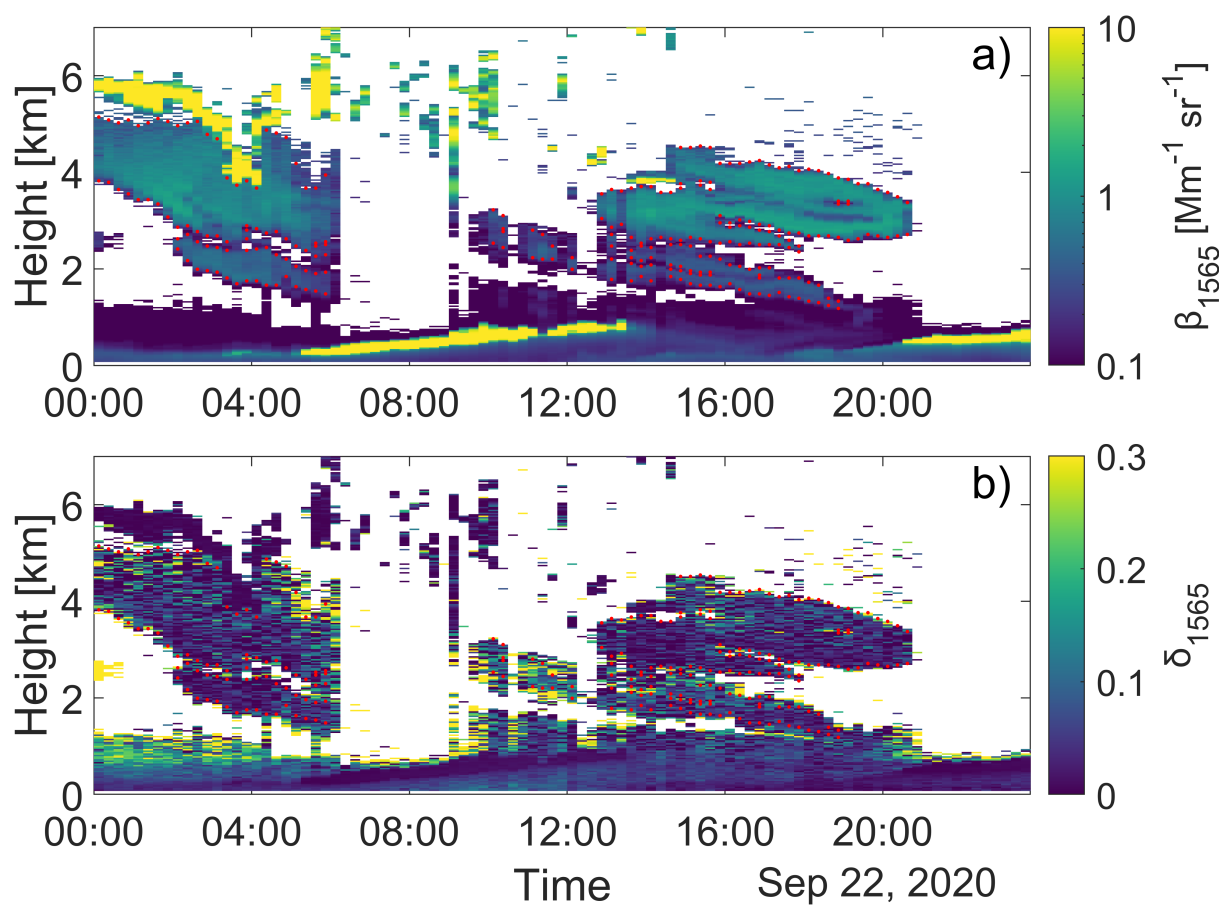


Figure 6. Time-height plot of a) β_{1565} and b) δ_{1565} measured in Kumpula 22 September 2020, with the HALO Doppler lidar. The red dots indicate the boundaries of the smoke layer. The temporal resolution corresponds to 15 minutes.

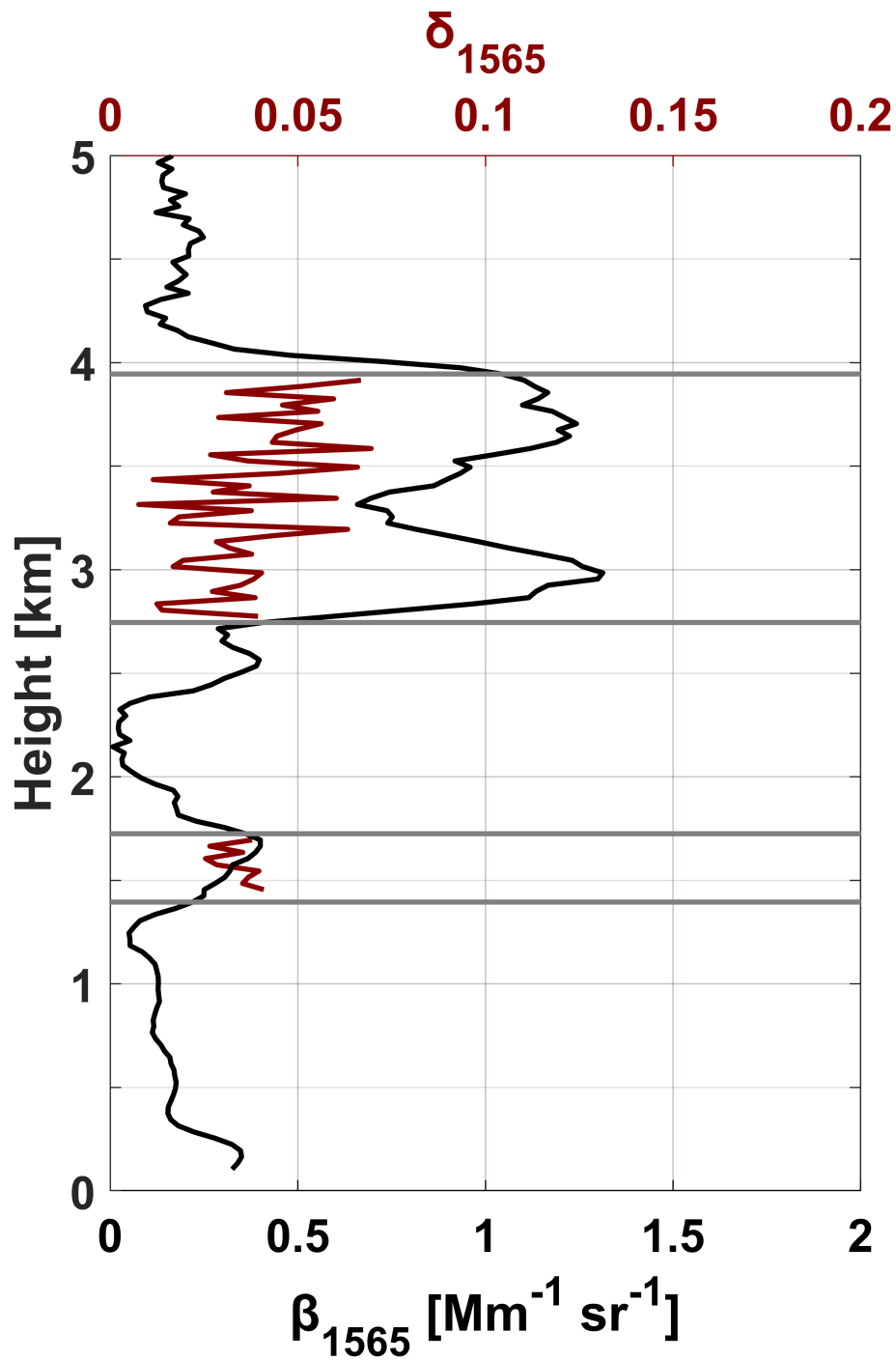


Figure 7. Mean β_{1565} (black) and δ_{1565} (dark red, for the smoke layers only) vertical profiles accounting for a temporal resolution of 1 hour starting at 17:00 UTC. The smoke layer base and top heights are indicated by gray horizontal lines.

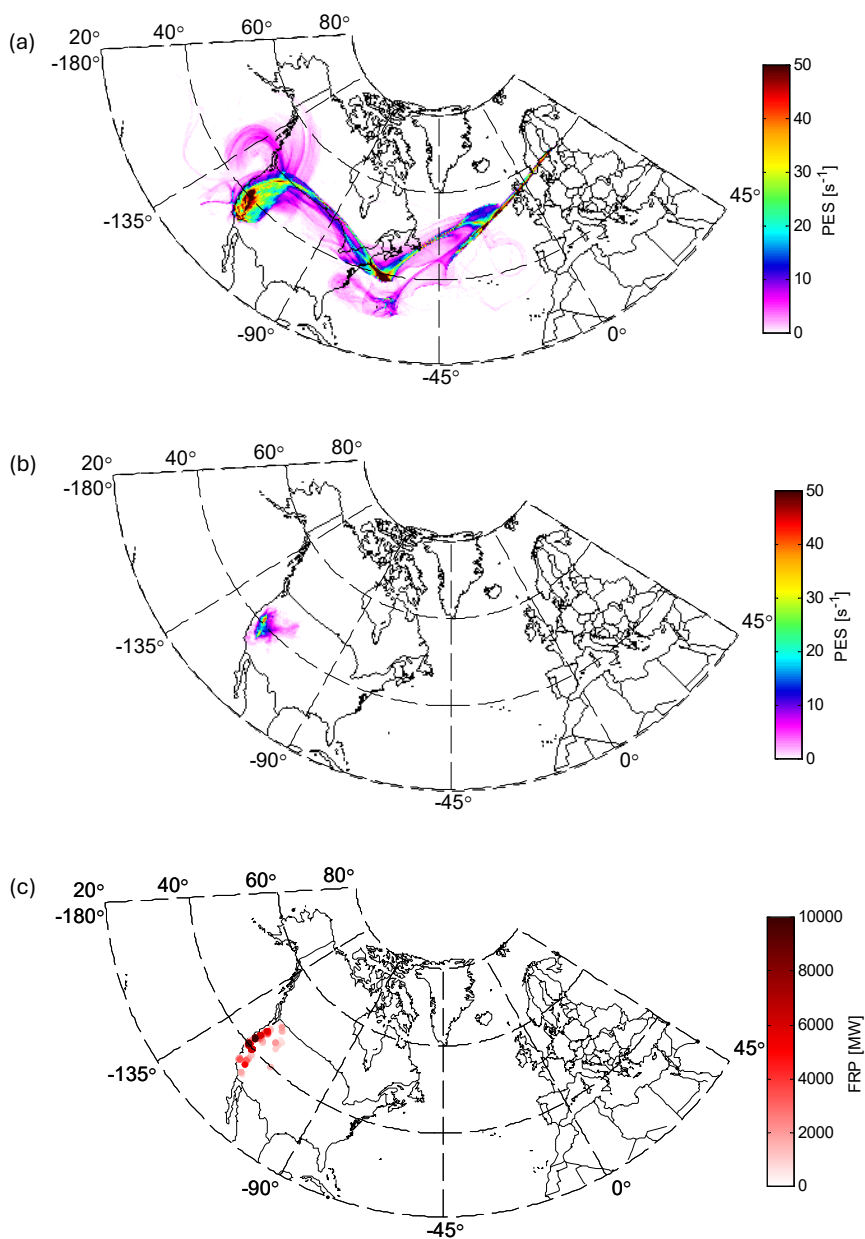


Figure 8. Air mass history for the Kumpula case on 22 September 2020 in Finland. (a) Sum of PES at all heights accounting for 16 days back in time. (b) Sum of PES for < 1 km a.g.l. for 16 days back in time. (c) MODIS observations of FRP > 500 MW for the time period 8 to 12 September 2020.

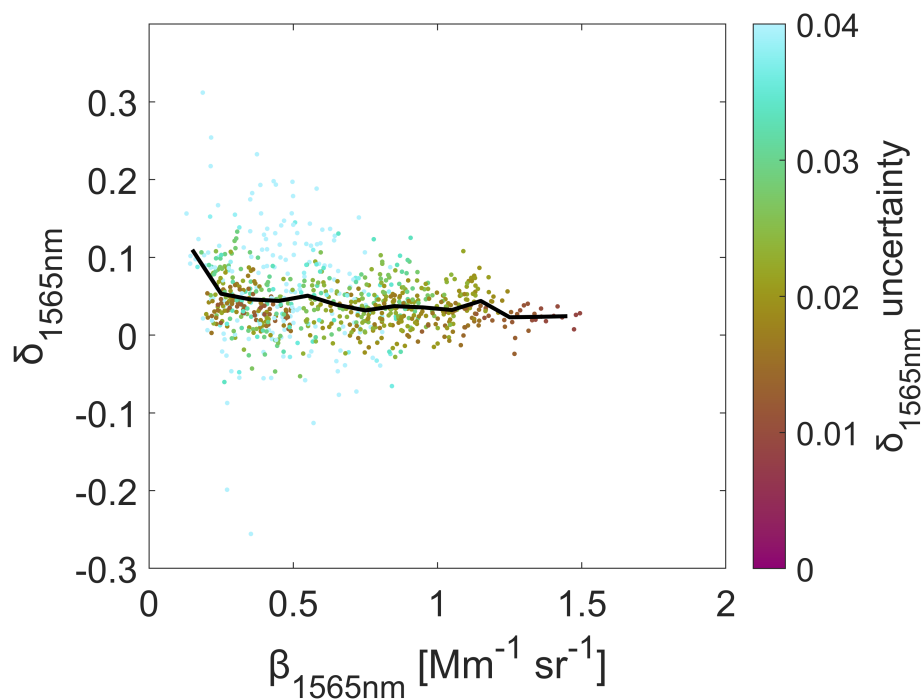


Figure 9. Scatterplot of β_{1565nm} versus δ_{1565nm} at the long-range transported smoke plume layer extracted from hourly lidar data. The black line shows the mean δ_{1565nm} binned every $0.1 \text{ Mm}^{-1} \text{sr}^{-1}$. The color indicates the absolute uncertainty of δ_{1565nm} .

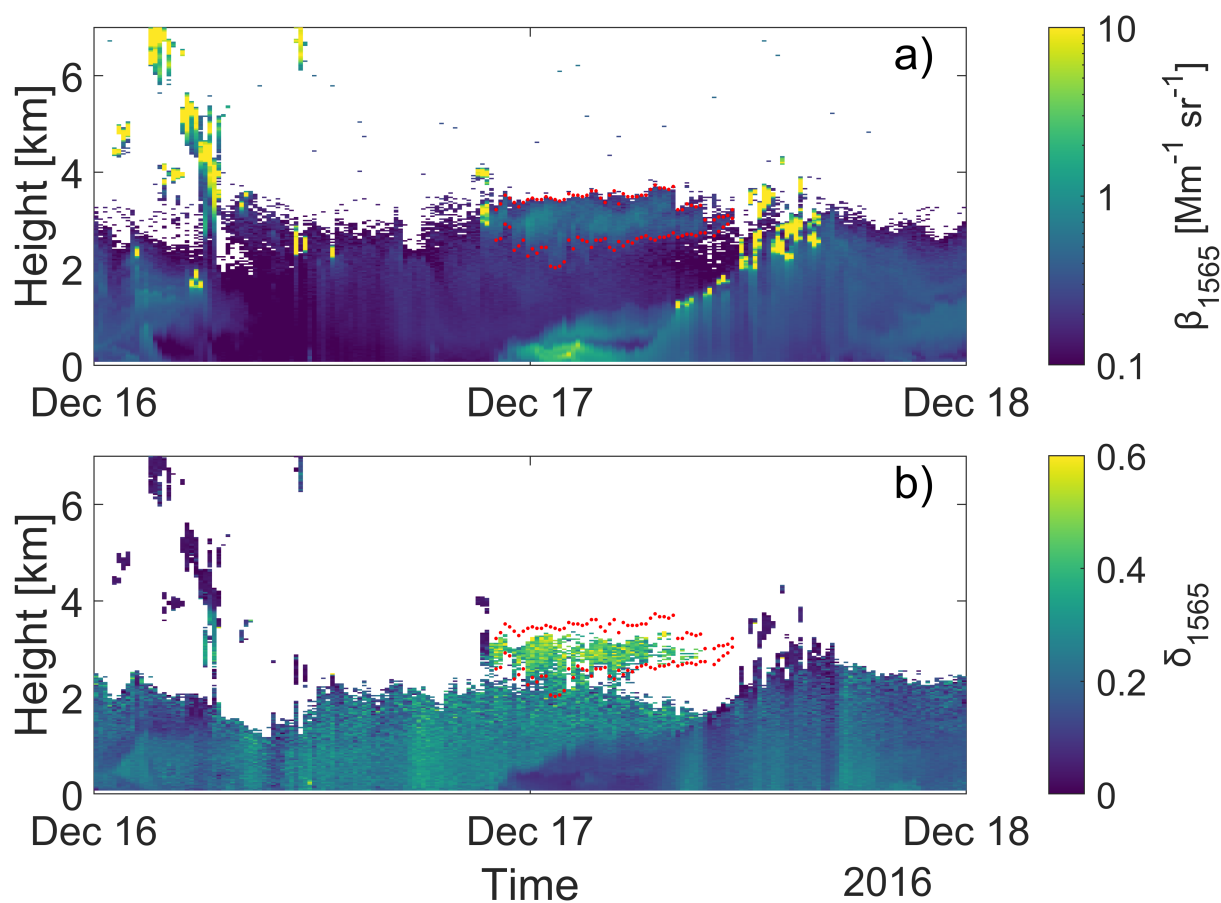


Figure 10. Time-height plot of a) β_{1565} and b) δ_{1565} measured between 16th and 17th of December 2016 in Welgegund, South Africa, with the HALO Doppler lidar. The red dots indicate the boundaries of the smoke layer. The temporal resolution corresponds to 15 minutes.

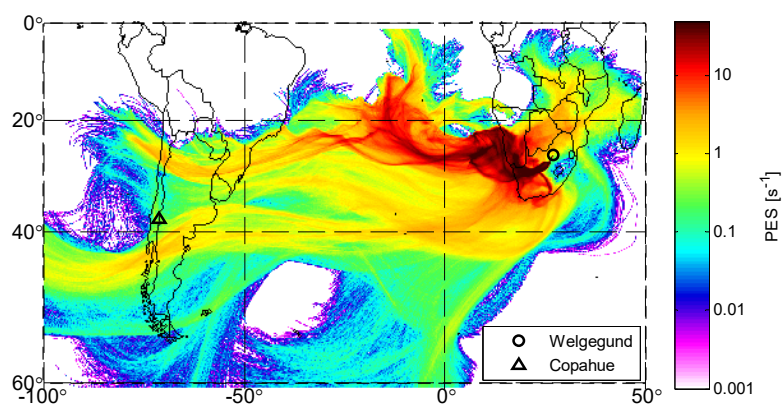


Figure 11. FLEXPART PES summed up over all heights accounting for 14 days back in time for the Welgegund case in South Africa on 17 December 2016.

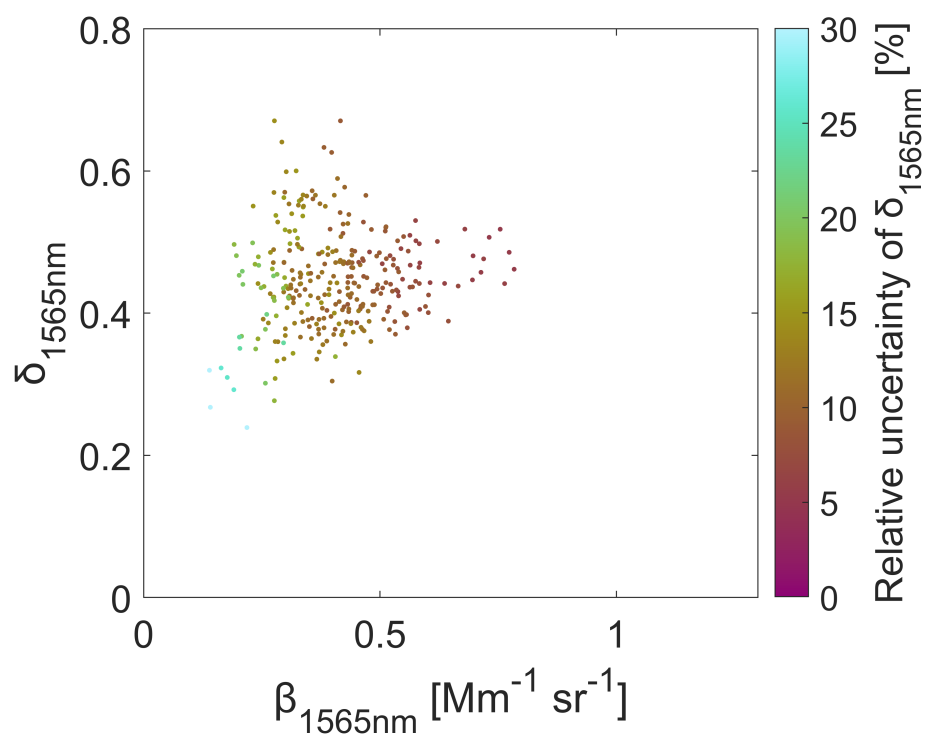


Figure 12. Scatterplot of $\beta_{1565\text{nm}}$ versus $\delta_{1565\text{nm}}$ at the volcanic plume layer extracted from hourly lidar data. The color indicates the relative uncertainty of $\delta_{1565\text{nm}}$.



Table 1. Depolarization ratio of aerosol types at 1565 nm.

| | δ_{1565} | Reference |
|-----------------|-------------------|-------------------------|
| Polluted marine | 0.009 ± 0.003 | Vakkari et al. (2021) |
| Fresh smoke | 0.017 ± 0.004 | This study |
| Aged smoke | 0.04 ± 0.02 | This study |
| Pine pollen | 0.26 ± 0.03 | Filioglou et al. (2023) |
| Desert dust | 0.30 ± 0.02 | Vakkari et al. (2021) |
| Birch pollen | 0.33 ± 0.04 | Filioglou et al. (2023) |
| Volcanic ash | 0.45 ± 0.05 | This study |

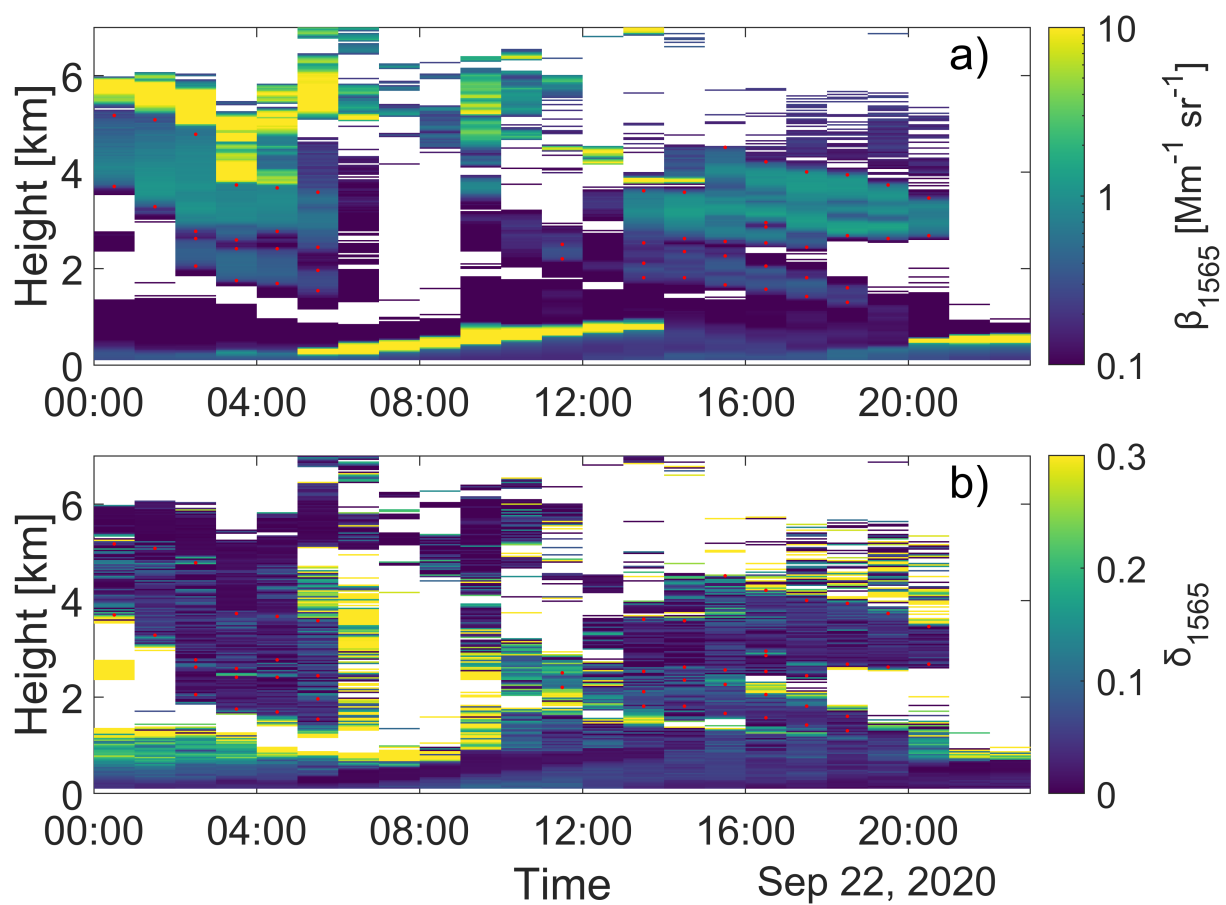


Figure A1. Similar plot to Figure 6 for a temporal averaging of 1 hour.

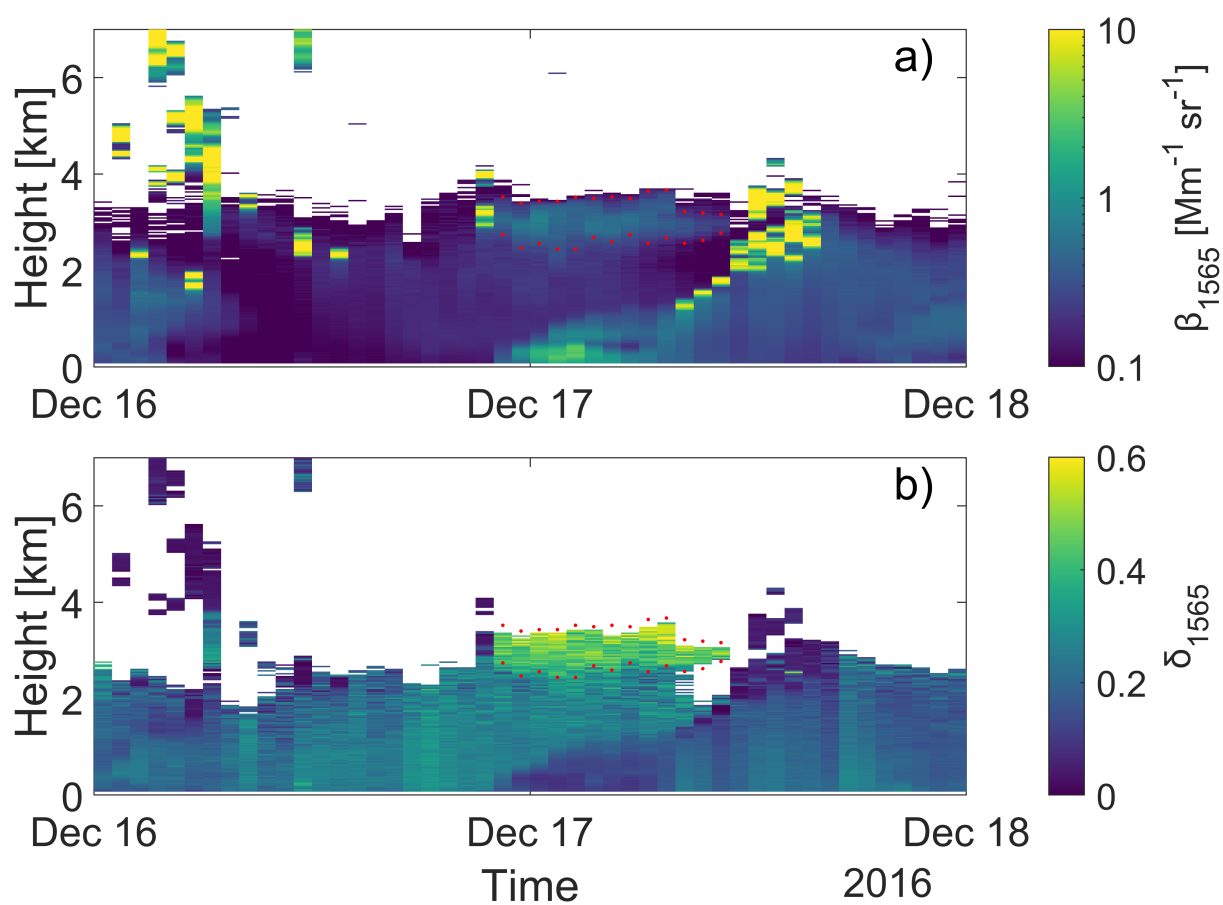


Figure A2. Similar plot to Figure 10 for a temporal averaging of 1 hour.